Terahertz Laser Vibration−Rotation Tunneling Spectroscopy and Dipole Moment of a Cage Form of the Water Hexamer

K. Liu,[†] M. G. Brown, and R. J. Saykally*

Department of Chemistry, University of California, Berkeley, California 94720

Received: March 3, 1997; In Final Form: June 3, 1997[⊗]

Tunable terahertz laser vibration−rotation-tunneling spectroscopy has been employed to characterize the structure and hydrogen bond network rearrangement dynamics of a cage form of the water hexamer having eight hydrogen bonds. The isolated clusters are produced in a pulsed supersonic slit jet. Striking similarities are found between the structure and the average interoxygen distance R_{O-O} (2.82 Å) of the hexamer cage and those of the basic unit of ice VI. The hybrid perpendicular band of b- and c-types is observed near 2.491 THz (83.03 cm^{-1}) and rationalized to originate from the torsional motions of the two single-donor single-acceptor monomers about their donor hydrogen bonds, thereby causing changes in the dipole moments from each monomer to be orthogonal to each other as well as to be perpendicular to the approximate symmetry *a*-axis. Triplet spectral patterns accompanying each rovibrational transition with line spacings of 1.9 MHz and intensity ratios of 9:6:1 are attributed to the degenerate quantum tunneling that involves the exchange of protons within two similar monomers of the cluster. The Stark effect of the degenerate asymmetry doublets of $K_a \geq 3$ has been analyzed to yield vibration- and (J,K_a)-dependent electric dipole moment components ranging from 1.82 to 2.07 D along the *a*-axis of this near prolate rotor. The selection rules establish that this dipole moment component preserves the sign upon vibrational excitation. A reasonable agreement is found between the dipole measurement and the results of a model calculation using an iterated induction expansion including the quadrupole-induced dipole. The same model has also been applied to extract the individual monomer dipole moments for the dimer and the cage and cyclic hexamers. The trends of two molecular properties—the contraction of the R_{O-O} distance and enhancement of the average individual monomer dipole with increasing cluster size up to the cyclic hexamer—are found to converge exponentially to the bulk phase values. In both cases, the cage properties deviate from the trends established by the dimer and cyclic clusters.

I. Introduction

The quest to accurately model the hydrogen-bonding inter-actions that dominate the structure and properties of water continues to be one of the important challenges in chemistry. To this end, studies of the structures and dynamics of water clusters are of importance for developing a detailed microscopic understanding of condensed phase phenomena. There is general agreement among numerous theoretical and experimental investigations of the water dimer,[1] first characterized spectroscopically by Dyke and Muenter in 1974.[2] For larger clusters, a growing number of ab initio and empirical calculations address the geometries and energetics, whereas detailed experimental characterizations of these systems have only begun to appear very recently.[3] Tunable terahertz laser vibration−rotation-tunneling (VRT) spectroscopy has emerged as a powerful tool for quantifying the structures and hydrogen bond rearrangement dynamics of small water clusters at an unprecedented level of accuracy.[4]

It has been well established that the global minimum on the intermolecular potential surface (IPS) of the water dimer corresponds to a near-linear one-dimensional (1-D) hydrogen-bonded complex. For the trimer, tetramer and pentamer, the lowest energy structures have been shown to be quasiplanar (2-D) monocyclic rings with each monomer acting as a single-donor and single-acceptor of hydrogen bonds.[5−13] Higher clusters such as heptamer[14] and octamer[15] are predicted to form

3-D noncyclic hydrogen-bonded networks at low internal temperatures by a large number of theoretical calculations. The hexamer represents a transition wherein the cyclic structures become less stable than the three-dimensional forms, which have a larger number of somewhat weaker (strained) hydrogen bonds.[16,17] Characterization of the structure and dynamical properties of the water hexamer is therefore of special interest.

The water hexamer has been the subject of numerous theoretical studies employing ab initio methods,[16−21] dynamics simulations,[8,22] and other techniques[12,13,23,24] that are based on model potentials. All have reported several low-lying structures with differences in the binding energies between the monocyclic and noncyclic conformations being less than 0.5 kcal/mol, but different relative stabilities are predicted at different levels of theory. High-level ab initio calculations of Jordan and co-workers[16,17] have predicted that the 3-D prism and cage hexamers lie several tenths of a kcal/mol below the monocyclic ring and that the cage appears as the most stable form of $(H_2O)_6$. As shown in Figure 1, similar conclusions regarding the stability ordering have been reached by Gregory and Clary[25] using diffusion quantum Monte Carlo (DQMC) simulation with a realistic model potential of Millot and Stone.[26] Direct comparison of structural parameters between DQMC calculations and experiment can be made since the former explicitly considers the effect of vibrational averaging, which is important in weakly bound aggregates possessing large amplitude motions even at the zero-point level.

Early molecular beam electric deflection experiments[27,28] and infrared (IR) vibrational predissociation spectroscopy pioneered by Lee and co-workers[29] suggest that the most stable water polymers from trimer through hexamer adopt cyclic structures.

---

† Present address: Department of Chemistry, University of Southern California, CA 90089.

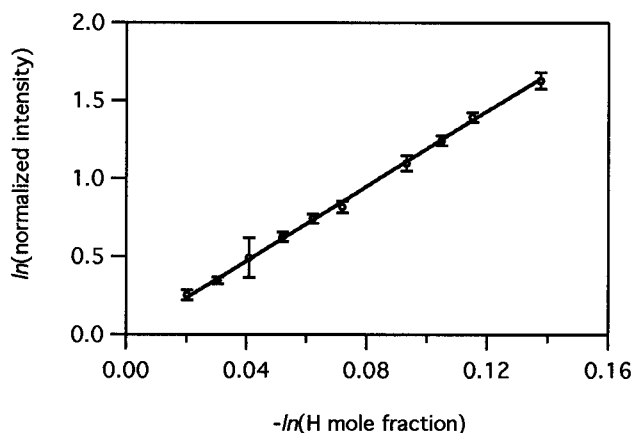* To whom correspondence should be addressed.
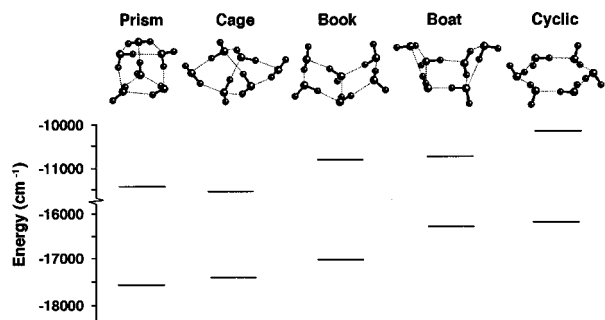
Figure 1. Five lowest-energy structures of the water hexamer and their relative stabilities predicted by Gregory and Clary using DQMC simulation with a water−water potential including nonpairwise additive corrections.[25] Values of D_e (lower lines, relative to 6 free water molecules) and D_0 (upper lines) are shown. The ZPE ($= D_0 - D_e$) calculations show that the cage structure is more stable than the prism by 62 cm^{-1} even though the latter is below the former by 213 cm^{-1} at potential minimum.


Figure 2. The logarithmic plot of the normalized signal intensity versus the H mole fraction used to establish the (water cluster) size of the spectral carrier. Each data point contains at least 10 normalized intensity measurements.

Coker, Miller, and Watts have observed IR predissociation spectra of large water clusters resembling that of liquid water in the 3000−3800 cm^{-1} O−H stretch region.[30] Employing a modified IR predissociation method, Pribble and Zwier[31] recently reported the first convincing spectroscopic evidence for noncyclic water clusters formed within the benzene−$(H_2O)_n$ complexes with $n = 6$ and 7. Vibrational predissociation broadening, however, precluded the acquisition of detailed structural parameters from these experiments.

The present study extends our previous[25] analysis of the VRT spectrum of the cage form of water hexamer and presents the determination of its dipole moment component by means of Stark effect measurements. A vibrationally averaged cage structure is established through the experimental rotational constants, which is corroborated by the electric dipole property deduced from the Stark splittings. On the basis of the observed structure, the origin of the intermolecular vibration observed in this work is assigned to predominantly torsional motions of the doubly bonded monomers within the cluster. Well-resolved quantum-tunneling splitting patterns associated with each rovibrational transition have allowed us to quantify the facile hydrogen-bond rearrangement dynamics, which are found to be common in small water clusters such as the dimer,[1,32,33] trimer,[34−39] tetramer,[40] and possibly the pentamer.[41] Mechanisms for such structural rearrangement dynamics are postulated with the aid of the molecular symmetry (MS) group G_4. Finally, trends in the interoxygen distance R_{O-O} and the individual water monomer dipole moment as a function of the cluster size, extracted from experimental parameters up to the hexamer, are shown to exhibit rapid convergence toward the corresponding properties of bulk water.

II. Experimental Section

The Berkeley terahertz laser spectrometer and its recent improvements have been described in detail elsewhere.[42,43] The size of a given water cluster responsible for an observed absorption feature was determined from an isotope mixture test described previously,[34] wherein the absorption line intensity was measured as a function of the H mole fraction in the H_2O + D_2O mixture employed for the production of water clusters. Careful intensity normalization[44] was performed by measuring the signals alternately between an isotope mixture and a pure reference sample. The logarithm of normalized intensities plotted against the H mole fraction (Figure 2) established a cluster size of 5.99 ± 0.15 to 95% confidence, hence clearly establishing the hexamer as the spectral carrier. All the spectral lines reported in this work have been tested with a simplified version of this method, wherein only one isotope mixture (84% H mole fraction) was used. The above test was particularly useful to identify signals observed from different sizes of water clusters found in a congested spectral region.[44] In addition to Ar, He, and first-run Ne (70% Ne in He) were also used as carrier gases to confirm that the absorption was indeed due to a pure water cluster.

The Stark effect of the hexamer VRT transitions was measured by applying uniform dc electric fields to the interaction region between the multipassed laser beam and the planar supersonic jet, which lies in the horizontal plane. The laser polarization (intrinsically horizontally polarized) was characterized with a metal wire polarizer in front of the detector to ensure that it is not degraded after multipassing. Two kinds of electrodes were employed to align the DC field vector either parallel or perpendicular to the laser polarization, allowing $\Delta M = 0$ or $\Delta M = \pm 1$ Stark transitions to occur, respectively. For the $\Delta M = 0$ measurements, the electric field was applied between the flat front surface of the slit nozzle body[43] and an electroformed nickel mesh (50 lines/in., Buckbee-Mears Co.) placed downstream of the supersonic expansion in attempt to minimize shock wave effects on the jet. For the $\Delta M = \pm 1$ Stark measurements, a pair of parallel hand-polished aluminum plates applied with opposite potentials (±V) were placed horizontally above and below the planar jet; situated slightly away from the electrode assembly, the nozzle body was grounded. The approximate uniformity (>95%) of the electric field in the laser-jet interaction region for both electrode arrangements was verified with a computer (MacSimion version 2.0) simulation. The lack of an accurate field calibration implies a few percent underestimate in the dipole moments thus determined. Electrical breakdown occurred at a field strength higher than 45 V/cm with the chamber background pressure at 30 mTorr and Ar as the carrier gas, which restricted Stark measurements in the terahertz spectral region to molecules with large dipole moments and fast pseudo-first-order electric field tuning.

III. Results

1. Spectral Assignments. Several factors lead to the assignment of the observed spectrum [(Figure 3A, spectrum 1)] to that of a near-prolate asymmetric rotor. The series of Q branch progressions clearly identified in the spectrum as the successive K subbands is indicative of a perpendicular ($\Delta K = \pm 1$) type of transition for a symmetric top-oblate or prolate. On the basis of a symmetric top Hamiltonian, a preliminary

Cage Form of the Water Hexamer

J. Phys. Chem. A, Vol. 101, No. 48, 1997 **8997**
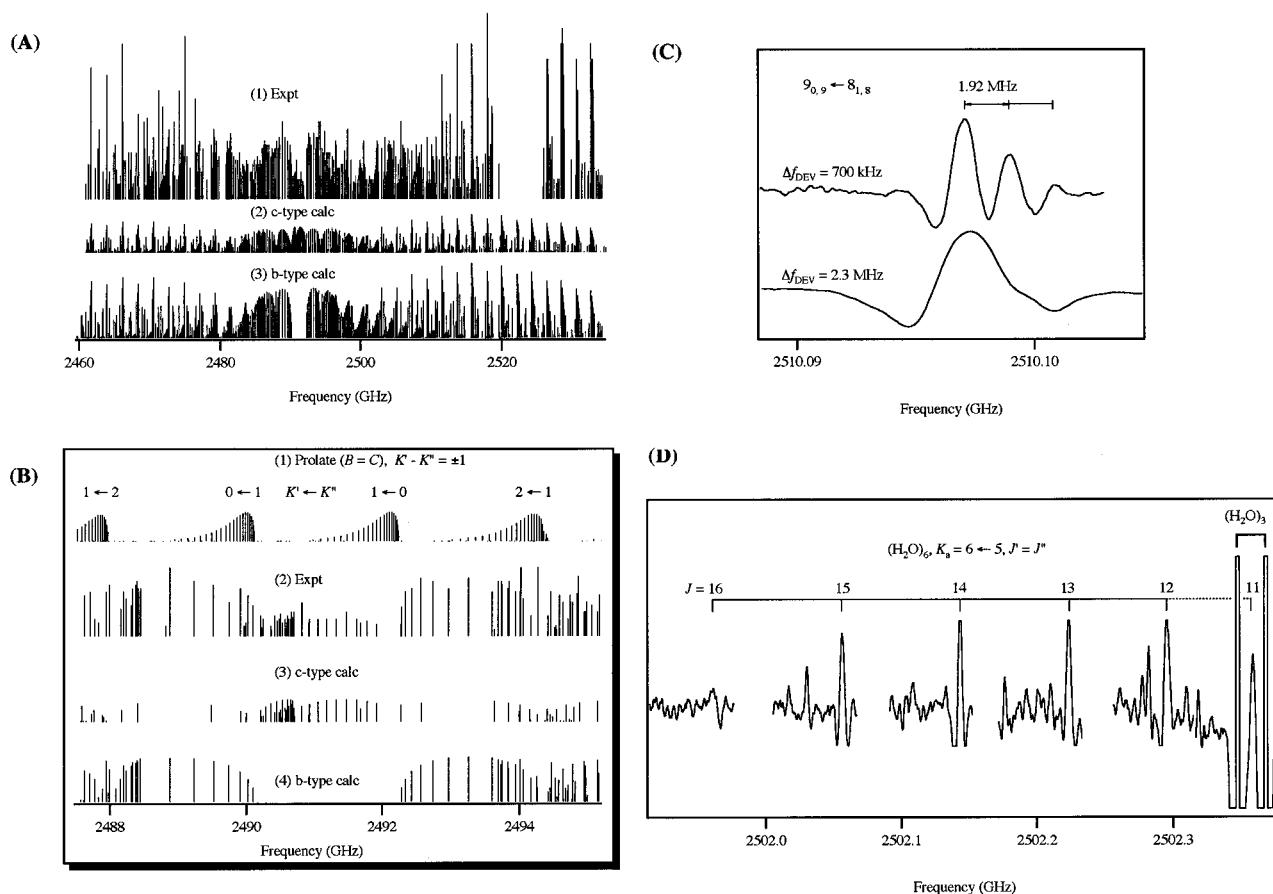
Figure 3. The observed and calculated VRT spectra of the near-prolate $(H_2O)_6$ cluster. (A, spectrum 1) The overall experimental stick spectrum can be decomposed into bands of (A, spectrum 2) c-type and (A, spectrum 3) b-type, which are calculated using the molecular constants in Table 1. The difference between the b- and c-type transitions can been most easily identified near the region of band origin as expanded in the inset B, wherein a rigorous prolate spectrum (B, spectrum 1) calculated with its rotational constants B'' ($=C''$) and B' ($=C'$) equal to the corresponding values of $(B + X)/2$ of the asymmetric cage is also displayed to show the relative red and blue shifts of the low K_a stacks in the b-type subbands (B, spectra 2 and 4) caused by the asymmetry doubling. (B, spectrum 3) The calculated c-type transitions near the band origin region. **(C)** The actual experimental spectrum of R(8), $K_a = 0 \leftarrow 1$ illustrates the triplet tunneling pattern (top trace resolved with a modulation deviation Δf_{DEV} of 700 kHz) accompanying each rovibrational transition. The bottom shows the same peak unresolved with $\Delta f_{DEV} = 2.3$ MHz, which was normally used in our experiments. **(D)** A survey scan of 462 MHz showing part of the $\Delta K_a = 6 \leftarrow 5 Q$ branch progression of the cage $(H_2O)_6$. The triplet patterns were not intended to be resolved. The H_2O trimer signals partially obscuring the Q(11) transition of $(H_2O)_6$ were saturated.

estimate of the rotational constants can be made from the measured spacings (2185 MHz) between the corresponding Q(J) lines of adjacent K subbands, which equals 2(B − C) for an oblate or 2(A − C) for a prolate top, neglecting distortion effects and the rotational constant differences between the ground and excited states. Assuming a near-planar ($B \sim 2C$) oblate top would yield a B constant of $\sim$2.19 GHz, a number that is too large for a cyclic S_6 hexamer. The B constant for this geometry should be 1.21 GHz, as extrapolated from the experimentally derived trend of interoxygen distance R_{O-O} for the cyclic water clusters up to the pentamer.[44] Nor can this correspond to a cyclic pentamer, albeit the estimated B constant (from the same R_{O-O} trend) for $(H_2O)_5$ is 1.95 GHz, because (a) a cyclic pentamer, $(D_2O)_5$, observed previously [41] did not give rise to a detectable Stark effect at the electric field attainable in this work due to its small vibrationally averaged dipole moment (<1 D), and (b) the sextet tunneling pattern expected for $(H_2O)_5$[45] does not agree with the triplet observed for each rovibrational transition, even when considering intensity perturbations. In fact, a calculation including both the Boltzmann ($T_{rot} = 6$ K) and Hönl−London factors for such an oblate top produced a spectrum grossly different from that observed, in terms of the intensity profiles between the P, Q, and R branches and particularly for the profile within each Q branch subband. Finally, from the apparent progression of the strong P and R branch lines, a $\sim$2B spacing of 2.1 GHz can be assumed. A

combination of this 2B spacing with the hypothesized 2(B − C) of 2.19 GHz rules out the possibility of the observed spectrum being that of an oblate rotor, since this would lead to $C \sim 0$ which does not correspond to a physical object. In contrast, the simulated prolate top spectrum based on 2(A − B) $\sim$ 2.19 GHz and 2B $\sim$ 2.1 GHz can qualitatively reproduce our measurements; the discrepancy is attributed to a slight asymmetry ($B \neq C$) of the spectral carrier.

The detailed assignments of the b-type transitions and the asymmetry doubling were realized by recognizing the Q branch progressions of the low K subbands, as shown in Figure 3, spectrum 2. The Q branches of the $\Delta K_a = 1 \leftarrow 0$ and $\Delta K_a = 0 \leftarrow 1$ subbands can be easily identified by the two repelling progressions prominent near the 2.491 THz region [Figure 3B, spectrum 2)]; they do not exhibit asymmetry doubling because the nondegenerate K_a' or $K_a'' = 0$ levels are involved. Transitions between two nonzero low K stacks have exhibited resolvable asymmetry doubling, e.g., in the regions near 2488.0 ± 0.5 GHz and between 2493.6 and 2494.7 GHz, as shown in Figure 3B, spectra 2 and 4. When compared to a simulated spectrum in the prolate limit (Figure 3B, spectra 1), the $\Delta K_a = 1 \leftarrow 0$ subband (starting near 2492.3 GHz in Figure 3B, spectra 2 or 4) is found to be more blue-shifted for the corresponding Q(J) lines, whereas the $\Delta K_a = 0 \leftarrow 1$ subband (starting near 2490.1 GHz in Figure 3, spectra 2) is more red-degraded. This suggests the transitions must either terminate in or originate

TABLE 1: Molecular Constants (in Megahertz) from Fitting of the 423 VRT Transitions (Available in Archival Form) of the Cage Hexamer Using a S-Reduced Watson Hamiltonian[a]

	Molecular Constants	
	ground state	excited state
A	2162.12(13)	2153.61(15)
B	1129.07(5)	1127.78(4)
C	1066.88(5)	1063.43(5)
D_{JK} (10^{-3})	−2.21(89)	−2.5(10)
D_K (10^{-3})	8.3(15)	−3.6(30)
d_1 (10^{-4})	4.28(92)	3.03(94)
d_2 (10^{-4})	−1.43(46)	−1.97(42)
H_{JK} (10^{-6})	5.7(18)	5.1(19)
H_{KJ} (10^{-5})	−5.36(61)	−4.05(70)
H_K (10^{-5})		−8.2(21)
ν_0 (band origin)	2 491 202.87(88)	

	Correlation Matrix																			
A''	1.00																		
B''	0.11	1.00																	
C''	−0.01	−0.10	1.00																
A'	0.81	0.12	−0.06	1.00															
B'	0.12	0.83	0.02	0.06	1.00														
C'	−0.05	0.01	0.86	−0.01	−0.10	1.00													
ν_0	0.14	0.10	0.13	−0.21	0.04	−0.09	1.00												
D_{JK}''	0.66	0.04	0.05	0.56	0.06	0.03	0.03	1.00											
D_{JK}'	0.51	−0.05	0.01	0.49	0.08	0.08	−0.26	0.87	1.00										
D_K''	0.61	−0.01	−0.16	0.46	0.00	−0.20	0.11	−0.03	−0.08	1.00									
D_K'	0.28	0.09	−0.12	0.62	−0.08	−0.11	−0.06	−0.08	−0.27	0.46	1.00								
d_1''	−0.07	−0.57	0.73	−0.08	−0.47	0.59	0.06	−0.02	−0.05	−0.11	−0.05	1.00							
d_1'	−0.10	−0.46	0.57	−0.05	−0.58	0.72	−0.11	−0.03	0.04	−0.15	−0.08	0.81	1.00						
d_2''	0.01	−0.15	0.08	0.02	−0.12	0.00	0.01	−0.01	−0.07	0.04	0.08	0.11	−0.10	1.00					
d_2'	0.00	−0.15	−0.04	0.01	−0.13	0.05	−0.15	0.00	0.11	0.01	−0.07	−0.09	0.09	0.34	1.00				
H_{JK}''	0.13	−0.05	0.17	0.18	−0.05	0.18	−0.04	0.67	0.61	−0.57	−0.23	0.17	0.18	−0.02	−0.01	1.00			
H_{JK}'	0.17	−0.06	0.18	0.22	−0.03	0.15	−0.03	0.67	0.64	−0.49	−0.21	0.19	0.14	0.02	−0.04	0.97	1.00		
H_{KJ}''	0.55	0.06	−0.10	0.37	0.09	−0.15	0.11	0.16	0.09	0.84	0.27	−0.15	−0.19	0.04	−0.01	−0.58	−0.50	1.00	
H_{KJ}'	0.32	0.00	−0.14	0.26	0.09	−0.03	−0.28	0.10	0.34	0.52	−0.05	−0.20	−0.04	−0.10	0.18	−0.46	−0.46	0.69	1.00
H_K'	0.07	0.10	−0.02	0.41	−0.08	−0.05	0.03	−0.05	−0.30	0.09	0.88	0.03	−0.05	0.10	−0.11	0.04	0.06	−0.07	−0.46 1.00

[a] 2σ Uncertainties in the last digits of the parameters are given in the parentheses. The root-mean squares of the fit is 6.2 MHz. The correlation matrix for the 20 constants is also tabulated.

from the upper levels ($J = K_a + K_c$) of the K_a' or $K_a'' = 1$ asymmetry doublets; hence, both are consistent with a b-type transition. Fitting of these two subbands, together with the K_a'' > 4 subbands which approach the prolate limit better than those with $1 \leq K_a'' \leq 4$ (asymmetry doublets were distinctly resolved for these Q branch lines), yielded molecular constants which lead to the assignment of the remaining transitions, including those belonging to a different c-type band.

The c-type transitions are distinguishable from the b-types only at low K_a values wherein the asymmetry doublet splittings from 10 up to a few hundred MHz are clearly resolvable. Therefore, the c-type band is most prominent in the region close to the band origin, especially identified as the lines shown in Figure 3B, spectra 2 and 3, and between the two Q branches of the b-type $\Delta K_a = 1 \leftarrow 0$ and $\Delta K_a = 0 \leftarrow 1$ subbands. In fact, an accompanying c-type band was initially anticipated, based on the vibrational motions postulated for the origin of the b-type band, as discussed below.

A total of 423 transitions (available in archival form) were assigned to a b- (387 lines) and c-type (36) hybrid band of $(H_2O)_6$. Molecular constants determined in a nonlinear least-squares fit of all transitions of both types to an S-reduced Watson Hamiltonian are given in Table 1.

2. Structure Modeling. Guided by the ab initio low-energy structures of Jordan and co-workers[16,17] and other investigators,[8,18,19] as well as by DQMC simulations of the vibrationally averaged rotational constants for various isomers of the hexamer made by Gregory and Clary,[25] a cage hexamer model was constructed to extract structural parameters from the measured rotational constants. The starting geometry showing only the

centers of mass of the monomers is given in Figure 4. Initial guesses are made such that the center of mass separation R_{COM} is the same for all the hydrogen bonds and each monomer is considered as a point mass. Situated at the diagonal apexes of a compressed cube, the triply bonded monomers form a puckered tetramer. The extent of puckering is characterized by the height of the cube h. The following two inertial conditions are used to solve for h and R_{COM}:

$$I_a = 4m\left(\frac{R_{COM}^2\; h^2}{2}\right) \qquad (1)$$

$$\left(\frac{I_b^{-1} + I_c^{-1}}{2}\right)^{-1} = 4m\left(\frac{R_{COM}}{2}\right)^2 + 2m\left(\frac{h}{2} + \sqrt{\frac{R_{COM}^2 + h^2}{2}}\right)^2 \qquad (2)$$

where m is the monomer mass. Equation 1 describes the dependence of I_a on only the four triply bonded monomers; in this model, the a-axis passes through the two single-donor single-acceptor (DA, D for donor, A for acceptor: this notation will be used throughout the paper) water molecules. The single D, single A monomers contribute to the averaged moment of inertia perpendicular to the symmetry axis of the top through the second term in eq 2, wherein the first term arises from the puckered tetramer.

The R_{COM} thus obtained is 2.886 Å and h is 1.356 Å. But since the point-mass model overestimates the interoxygen distance according to our experimental R_{O-O} trend established for the dimer through the cyclic pentamer,[41] an empirical scaling factor of 0.977 is used to obtain R_{O-O} as 2.82 Å. With h being

Cage Form of the Water Hexamer

*J. Phys. Chem. A, Vol. 101, No. 48, 1997* **8999**
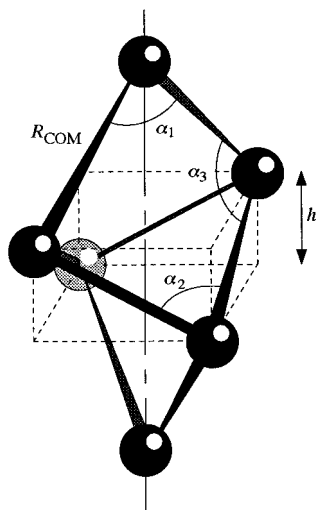
Figure 4. A model geometry for the cage hexamer. Only the centers of mass are shown. The lines also represent the hydrogen bond connectivity established between the monomers.

a less obvious structural parameter, various $O \cdots O \cdots O$ angles are calculated using R_{COM} and h. The $O \cdots O \cdots O$ angle (α_1) at the doubly bonded monomer and the angle (α_2) within the puckered tetrameric monomers are the same (77.24°) as a result of constraining R_{COM} to be identical for all the hydrogen bonds. A third $O \cdots O \cdots O$ angle (α_3), connecting the oxygens of DDA $\cdots$ DAA $\cdots$ DA or DAA $\cdots$ DDA $\cdots$ DA monomers, is 88.1°. Note that, relating closely to the $H \cdots O - H$ (both hydrogens bonded) angle, the $O \cdots O \cdots O$ angle is a measure of the deviation from the ideal tetrahedral bonding geometry established for the condensed phase water; an $O \cdots O \cdots O$ angle smaller than the 109.5° tetrahedral bonding angle is associated with a strain in the hydrogen bond. This is clearly manifested in the optimal structure of water pentamer wherein the slightly puckered pentagonal ring form is more stable than the cage or bicyclic arrangements,[46] which involve three- and four-membered rings despite the latter containing extra hydrogen bonds.

Due to vibrational averaging, the precise positions of the free hydrogens cannot be determined in this rigid model. Assuming a linear $O - H \cdots O$ bonding geometry, $O - H_{bonded} = 0.971$ Å, $O - H_{free} = 0.959$ Å, and a monomer bending angle of 104.5°, the asymmetry parameter κ calculated from the model structure is -0.95, compared with the experimental ground-state value κ'', -0.886; the discrepancy can be attributed to not only the inaccurate atomic positions, but also to the exclusion of dynamical averaging effects in the model. A calculation with the optimized coordinates of Gregory and Clary[47] produced $\kappa = -0.91$; their DQMC simulations[25] indicate that vibrational averaging is important for distinguishing between the rotational constants of different isomers. A much less sophisticated MC simulation[37] based on the approximate wave functions of the large amplitude vibrations has been performed for the water trimers to obtain structural parameters from the measured rotational constants; such an approach should also be applicable here—at least the agreement between the DQMC and the simple MC simulations tested on the vibrationally averaged R(O–O) distances of various water trimer isotopomers is excellent (within 0.3%).[48]

3. Nondegenerate Cage Hexamers: Vibrational Assignment. A set of four symmetrically inequivalent cage structures can be obtained by sequential flipping of the free O–H bond on each DA monomer from one side of an O–O–O plane to the other; the plane is formed by the oxygens of the DA monomer and the two neighboring molecules which are directly
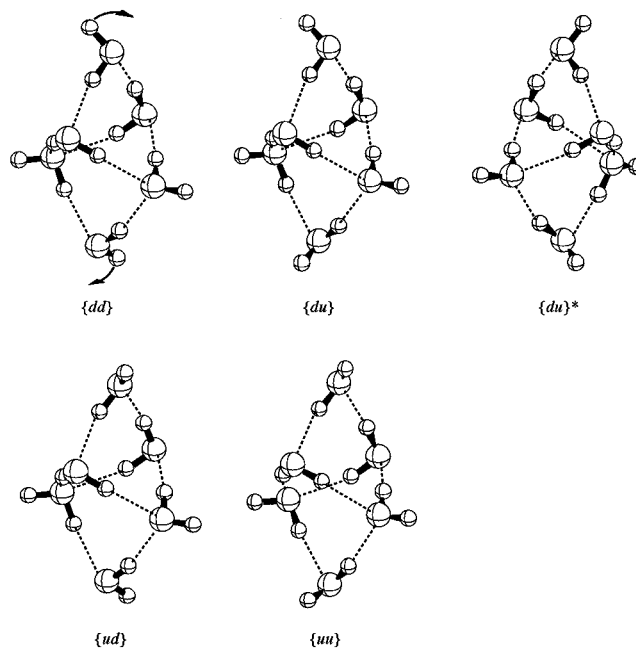
Figure 5. Four nondegenerate cage hexamers, {dd}, {du}, {uu}, and {ud}, produced by flipping the two doubly bonded monomers. A calculated[47] structure, {du}*, which is approximately enantiomeric to {du} in term of the hydrogen bond connectivity, is also shown. The two curved arrows next to the free hydrogens on {dd} indicate the directions of the flipping motion, which may be responsible for the observed perpendicular hybrid bands.

TABLE 2: Calculated Rotational Constants of the Four Cage Structures Interconnected through Flipping of the Free O–H Bonds on the Two DA Monomers[a]

	A/MHz	*B*/MHz	*C*/MHz
{dd}[b]	2133.2	1102.7	1074.7
{du}[b]	2134.1	1103.2	1075.4
{ud}[b]	2133.6	1102.1	1075.5
{uu}[b]	2133.4	1105.5	1079.0
{du}*[,c]	2280.8	1159.6	1109.6

[a] Notations are defined in the text; {du}* represents the approximate (due to the different methods used to obtain the two structures) enantiomeric form of {du}. [b] This work. [c] DQMC structure, rotational constants not averaged (see ref 47).

bonded to it. Two such planes associated with each DA monomer are found to be approximately orthogonal to each other, hence so are the trajectories of the two flipping O–H bonds. Analogous flipping motions identified for the trimer[34-36,49,50] can lead to isoenergetic enantiomers. The four cage hexamer structures linked by flipping are, however, inequivalent. Energetics calculations show that these structures are separated by ca. 50 cm^{-1}.[47] Extending the scheme for designating the interconnecting trimers: u (up) for a free H above the O–O–O plane, d(down) for H below the plane, we refer to the four cage structures (Figure 5) as {dd}, {du}, {ud}, and {uu} with each describing the state of the two DA monomers relative to the planes containing their donor O–H bonds. The dihedral angle between the free O–H bond and the O–O–O plane about which it flips is chosen to be approximately 50°, the value found for the trimer. As a comparison, we also give the results for an optimized cage structure obtained in a model potential-based calculation by Gregory and Clary;[47] this structure denoted as {du}* is enantiomeric to {du} denoted in this work, considering only the connectivity of the hydrogen bonds rather than the detailed structural parameters. Table 2 lists the rotational constants obtained for these five model structures, the coordinates of

9000 *J. Phys. Chem. A, Vol. 101, No. 48, 1997*

Liu et al.

TABLE 3: Character Table of the Permutation Group G_4[a]

G_4	E	(12)	(34)	(12)(34)
A_a	1	1	1	1
A_b	1	1	−1	−1
B_a	1	−1	1	−1
B_b	1	−1	−1	1

[a] Operation labels 1, 2, 3, and 4 refer to the hydrogen atoms shown in Figure 6.

TABLE 4: Tunneling Splitting Pattern Predicted for the Cage Hexamer under the Permutation Group G_4[a]

symmetry (spin weights)	relative tunneling energy	symmetrized eigenfunction
A_a (18, 72)	$\beta_1 + \beta_2 + \beta_3$	$(\phi_1 + \phi_2 + \phi_3 + \phi_4)/2$
A_b (6, 36)	$\beta_1 - \beta_2 - \beta_3$	$(-\phi_1 - \phi_2 + \phi_3 + \phi_4)/2$
B_a (6, 36)	$-\beta_1 + \beta_2 - \beta_3$	$(-\phi_1 + \phi_2 + \phi_3 - \phi_4)/2$
B_b (2, 18)	$-\beta_1 - \beta_2 + \beta_3$	$(\phi_1 - \phi_2 + \phi_3 - \phi_4)/2$

[a] The numbers in the parentheses are the nuclear spin weights given for $(H_2O)_6$ and $(D_2O)_6$, respectively. The tunneling matrix elements β_n's are determined to be negative (see text). The basis functions ϕ_n (n = 1, 2, 3, and 4) correspond to the localized wave function of the nth degenerate version of the cage hexamer (Figure 6).

TABLE 5: Line Strengths $\lambda_a(J\tau,J\tau')$ Used in the Stark Energy Calculations ($\tau = K_a - K_c$)

ground state ($\kappa'' = -0.8864$)		Excited state ($\kappa' = -0.8819$)	
asymmetry doublet ($J\tau - J\tau'$)	λ''	asymmetry doublet ($J\tau - J\tau'$)	λ'
$4_4 - 4_3$	7.1988	$3_3 - 3_2$	5.2485
$5_3 - 5_2$	5.8630	$5_5 - 5_4$	9.1655
$5_1 - 5_0$	3.2908	$6_2 - 6_1$	4.9447

which are also used in the dipole modeling presented below. As shown in Table 2, flipping of the light hydrogen atoms only changes the B and C rotational constants by a few MHz, the change in *A* constant is even less because the flipping hydrogens are near the *a*-axis.

The observed hybrid perpendicular band is consistent mainly with the flipping motions of the two DA monomers about their donor O−H bonds, which could be accompanied by the cooperative motions of other moieties. The dipole moment changes associated with the flipping are predominantly along the *b*- and *c*-inertial axes (see Table 9 below), thereby producing two types of mutually orthogonal perpendicular bands. Thus, the observed VRT band is likely to correspond to the transitions between the eigenstates that are supported by the above four nondegenerate structures linked by flipping; the resulting eigenfunctions must be quite delocalized.

4. Degenerate Structural Rearrangement Analysis: Tunneling Pattern. We now attempt to explain the triplet spectral fine structure observed for each rovibrational transition of the cage hexamer. The permutation−inversion (PI) symmetry group[51−53] is employed to rationalize the degenerate structural rearrangement dynamics, which is responsible for the observed splitting patterns. The procedure used here is similar to those well-established treatments for the water dimer[54] and trimer.[35,49]

There exist a number of low-energy nondegenerate isomers identified for the hexamer in previous calculations. For the high-resolution tunneling splitting patterns observed in this work, however, it is only necessary to consider the symmetrically equivalent or degenerate structures obtained through permutation of identical nuclei and space-fixed inversion, based on the fact that the two essential features, the line spacing (∼1.9 MHz) and intensity ratios (9:6:1), characteristic of the observed triplet pattern are invariant with respect to the rotational quantum numbers.

Here we address three fundamental points that argue against attributing the splitting to transitions within different nondegenerate structures, the first two in terms of the vibrational shift and rotational line spacings, the third concerning the intensity ratios. (1) For the calculated ∼50 cm^{-1} energy separations among the four nondegenerate cage structures (other forms of the hexamer are more widely separated from the cage),[47] it is unlikely that the vibrational shift from each conformation which would cause the triplet is only 1.9 MHz in a nonrigid system wherein vibrational anharmonicity dominates. (2) Even if the vibrational frequencies could be coincidentally identical, nondegenerate geometric structures, by the very definition, imply different vibrationally averaged molecular constants and hence different rotational spacings. Such differences should be manifested in the spectrum, especially at high *J* and *K* quantum numbers wherein the finite differences between molecular constants can be strongly amplified. (3) The intensity of an electric dipole transition is proportional to the product of the cluster number density, the nuclear spin statistical weight and the Boltzmann temperature factor. The spin weights of different isomers must be the same (equals overall number of

spin functions) due to their identical chemical composition; by symmetry, the nuclear spin weight can only be distributed among different symmetry species of the degenerate, rather than nondegenerate isomers. Therefore, the intensity ratios of rovibrational transitions attributed to nondegenerate structures would be subject to change upon experimental conditions (e.g., temperature) wherein the cluster distribution can be varied. Such a change was not observed in our experiments. Furthermore, it seems too coincidental that a closely spaced spectral multiplet caused by nondegenerate structures, after unusually satisfying the above vibrational and rotational requirements, could also match the *J*, *K* independent intensity ratios derived below for a degenerate tunneling process. All the above features, however, are completely explained by *degenerate* structural rearrangements.

Based on the two possible facile motions—"flipping" and "donor tunneling" (or "bifurcation") established for the water trimer,[35,49,50,55−59] we now deduce for the cage hexamer the appropriate MS group, the simplest group sufficient to explain the resolvable spectral features. The flipping motion mainly involves the low-barrier torsion (for the trimer, the zero-point level is above the barrier[56]) of a water molecule essentially about its donor O−H bond axis, whereas the "donor tunneling" generally refers to the exchange of the bound and free hydrogens within a monomer for which the transition state in the dimer[60] and the trimer[57] has a "bifurcated" hydrogen-bonding geometry. As shown in Figure 1, the equilibrium structure of the cage hexamer has C_1 point group symmetry. Flipping of the free O−H bonds in the two DA and the two DAA monomers results in inequivalent structures, therefore it is symmetry forbidden as regards the degenerate tunneling; such symmetry simplification has also been found in the mixed isotopic trimers[37] and in the tetramer.

The bifurcation pathway involves the breaking of a hydrogen bond and thus is associated with a higher barrier than is the flipping motion. Numerous theoretical[49,57,60,61] and experimental[34,62,63] work has characterized this bifurcation pathway and resulting tunneling features in smaller water clusters. It was recently found by van der Avoird and co-workers[58,59] that, in order to explain the detailed tunneling dynamics and Coriolis coupling in the trimer VRT spectra, the bifurcation pathway must involve the inversion operation (E^*); namely, it must be accompanied by flipping motions of the two nonbifurcating monomers. However, as reasoned for the mixed trimers,[37] when

Cage Form of the Water Hexamer

J. Phys. Chem. A, Vol. 101, No. 48, 1997 **9001**
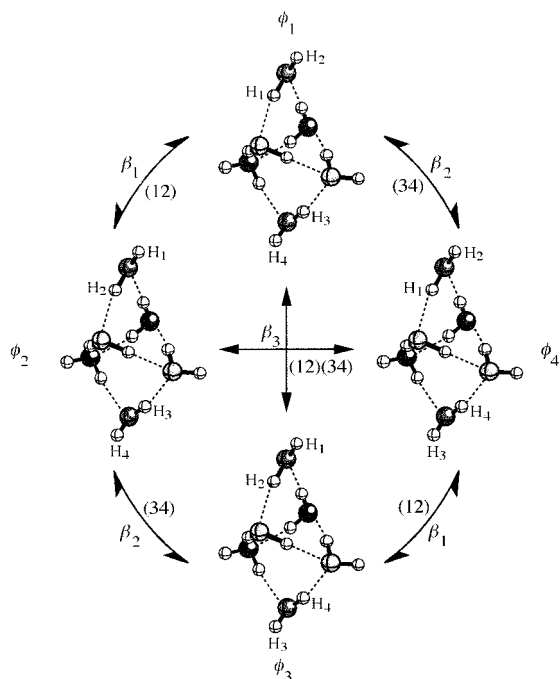
Figure 6. Four degenerate cage structures linked through the effective C_2 tunneling of two doubly bonded monomers. The off-diagonal tunneling matrix elements β_n ($n = 1-3$) connecting different localized wave functions ϕ_n ($n = 1-4$) are shown with the corresponding permutation operations defined in the text. Note that the flipping motion of the doubly bonded monomers does not yield degenerate structures that can be considered in classification of tunneling symmetries.

flipping becomes symmetry forbidden, the bifurcation tunneling may become an effective monomer C_2 rotation, which is intuitively expected to be associated either with a longer pathway or higher barrier (or both) than those found for the dimer and isotopically homogeneous trimer. Likewise, the cage hexamer donor tunneling studied here is postulated to undergo the effective C_2 rotation, with associated flipping motions being infeasible.

For the cage hexamer, the DA monomers, which are less constrained than the triply bonded DAA and DDA monomers, are most likely to undergo the C_2 tunneling. This assumption does not affect the following general conclusion. Here we shall consider the doubly bonded monomers. Due to the slight inequivalence between the two monomers—one is bonded to two DAA molecules and the other to two DDAs—each C_2 pathway is expected to experience slightly different barriers and thus to produce different tunneling matrix elements. Following the Hückel tunneling treatment of Wales,[49] we associate the tunneling matrix element β_1 with the symmetry operation 12, which permutes H_1 and H_2 (Figure 6), β_2 with the operation 34, and β_3 with the operation (12)(34). The operation (12)(34) corresponds to the concerted C_2 rotations of both DA monomers, and thus β_3 should be much smaller than β_1 and β_2 since this pathway involves the breaking of two hydrogen bonds. The group generated by the above symmetry operations is G$_4$, the character table of which is given in Table 3. The irreducible representations (irreps) are defined such that the capital letters A and B label the symmetric and antisymmetric species with respect to the operation 12, and the subscripts a and b accordingly to operation 34. Note that this group is a pure permutation group because the inversion operation associated with the flipping motion is not feasible.

To predict the symmetry properties and tunneling patterns of the cage hexamer from the properties of the group G$_4$, we consider the following basis set for the phenomenological

TABLE 6: Dipole a-Components (in Debye) Obtained from Fitting the Stark Patterns

	$3_3 \leftarrow 4_4$	$5_5 \leftarrow 4_4$	$5_5 \leftarrow 5_4$	$6_4 \leftarrow 5_3$
μ_a''	1.85	1.85[b]	2.07	1.82
μ_a''	1.89	1.99	1.99[b]	1.89
rms/kHz	50	56	15	36

[a] Transitions from which the dipoles are fit are labeled as $J'_{K_a'} \leftarrow J''_{K_a''}$. The uncertainties in the peak splittings were set to 50−70 kHz in the nonlinear least-squares fit. [b] Fixed to the values of common states in the fit.

TABLE 7: Structural and Electrical Properties of the Water Monomer Employed in the Induced Dipole Model Calculation[a]

		electrical properties	
structural parameters		polarizability/ $\times 10^{-24}$ cm^3	quadrupole moment/ $\times 10^{-26}$ esu
free R_{O-H}/Å	0.959	$\alpha_{aa} = 1.528$ [82]	$Q_{aa} = 2.63$ [83]
bound R_{O-H}/Å	0.971	$\alpha_{bb} = 1.468$ [82]	$Q_{bb} = -0.13$ [83]
H−O−H angle/deg	104.52	$\alpha_{cc} = 1.528$ [82]	$Q_{aa} = -2.50$ [83]

[a] Principal axes are defined in the text.

J-independent 2-D tunneling Hamiltonian H_{tun} with each degree of freedom corresponding to the state of a DA monomer. We define four localized states ϕ_1, ϕ_2, ϕ_3, and ϕ_4, corresponding to the structures **1**–**4** in Figure 6, respectively. The tunneling path between the four degenerate cage structures can therefore be established symbolically as

$$\phi_{m \neq n} = (12)\phi_n \quad \text{with} \quad m, n = (1, 2) \quad \text{or} \quad (3, 4) \quad (3)$$

e.g.,

$$\phi_1 = (12)\phi_2 \text{ or } \phi_2 = (12)\phi_1$$

$$\phi_{m \neq n} = (34)\phi_n \quad \text{with} \quad m, n = (2, 3) \quad \text{or} \quad (1, 4) \quad (4)$$

and

$$\phi_{m \neq n} = (12)(34)\phi_n \quad \text{with} \quad m, n = (1, 3) \quad \text{or} \quad (2, 4) \quad (5)$$

The tunneling matrix in the $\{\phi_n, n = 1-4\}$ basis is

$$\begin{pmatrix} H_{11} & \beta_1 & \beta_3 & \beta_2 \\ \beta_1 & H_{22} & \beta_2 & \beta_3 \\ \beta_3 & \beta_2 & H_{33} & \beta_1 \\ \beta_2 & \beta_3 & \beta_1 & H_{44} \end{pmatrix} \quad (6)$$
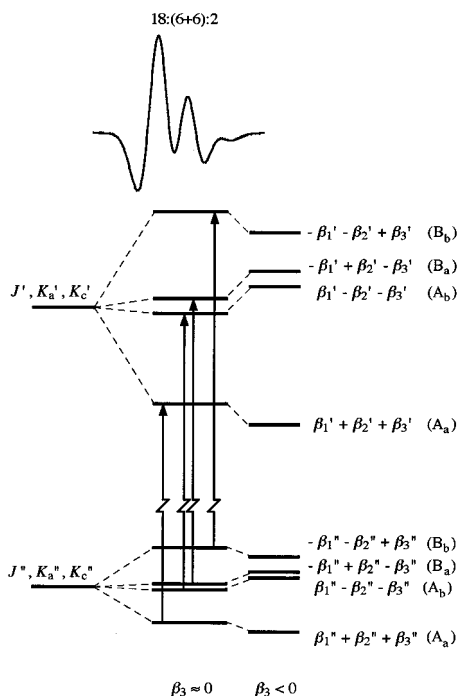
where $H_{nn} = \phi_n H_{tun} \phi_n$ and $H_{mm} = H_{nn}$ ($m \neq n$) due to structural degeneracy, with $m, n = 1-4$. On the basis of the connectivity defined above for the three possible tunneling operations, the tunneling matrix elements are expressed as

$$\beta_1 = \phi_n H_{tun}(12)\phi_n \quad (7)$$

$$\beta_2 = \phi_n H_{tun}(34)\phi_n \quad (8)$$

$$\beta_3 = \phi_n H_{tun}(12)(34)\phi_n \quad (9)$$

where $n = 1-4$. Note that a different definition of β_i was used in our previous paper[25] wherein β_i is the tunneling splitting, which is twice the tunneling matrix element defined here. The tunneling levels resulting from the H_{tun} matrix are listed in Table 4; schematic transitions between the VRT levels are shown in Figure 7 with the selection rule of $\Gamma_i \leftrightarrow \Gamma_i$ imposed.

18:(6+6):2

J', K_a', K_c'

$-\beta_1' - \beta_2' + \beta_3'$ (B$_b$)

$-\beta_1' + \beta_2' - \beta_3'$ (B$_a$)

$\beta_1' - \beta_2' - \beta_3'$ (A$_b$)

$\beta_1' + \beta_2' + \beta_3'$ (A$_a$)

J'', K_a'', K_c''

$-\beta_1'' - \beta_2'' + \beta_3''$ (B$_b$)

$-\beta_1'' + \beta_2'' - \beta_3''$ (B$_a$)

$\beta_1'' - \beta_2'' - \beta_3''$ (A$_b$)

$\beta_1'' + \beta_2'' + \beta_3''$ (A$_a$)

$\beta_3 \approx 0$ $\beta_3 < 0$

Figure 7. Schematic energy diagram illustrating the VRT transitions giving rise to the triplet spectral pattern (top trace) with the intensity ratios proportional to the nuclear spin weights (numbers shown atop the sample spectrum) of the tunneling state symmetries. The tunneling energies relative to the nontunneling limits are also given with the symmetry labels of the MS group G$_4$ in the parentheses. The energy levels (solid lines) are constructed with all β_n's being negative and β_3 being either negligible or finite; nonzero β_3 would lead to uneven spacings in triplet, in contradiction with the observed pattern.

The predicted quartet spacings are therefore given as follows:

$$\Delta\nu(B_b - B_a) = 2(-\beta_2' + \beta_2'') - 2(\beta_3' - \beta_3'') \quad (10)$$

$$\Delta\nu(B_a - A_b) = 2(-\beta_1' + \beta_2') - 2(-\beta_1'' - \beta_2'') \quad (11)$$

$$\Delta\nu(A_b - A_a) = 2(-\beta_2' + \beta_2'') + 2(\beta_3' - \beta_3'') \quad (12)$$

The spacing between the central doublet (A$_b$ and B$_a$ components) is expected to be small since the barriers to operations 12 and 34 are similar, i.e., $\beta_1 - \beta_2 \sim 0$ for both the ground and excited states. As this splitting becomes less than the instrumental resolution (2 MHz), the quartet collapses into a triplet of the intensity ratios of 18:(6 + 6):2 corresponding to the nuclear spin statistical weights of (H$_2$O)$_6$ (Table 4) associated with the A$_a$, A$_b$ ⊕ B$_a$, B$_b$ symmetries, respectively. This is believed to be the case observed for the cage hexamer in our VRT experiments.

By comparing the predicted tunneling pattern to the observed triplet, we can establish two qualitative constraints on the tunneling matrix elements. First, the two spacings in the observed triplet are approximately equal (within 100 kHz). This leads to

$$|\beta_3' - \beta_3''| < 25 \text{ kHz} \quad (13)$$

which is consistent with a high-barrier (12)(34) tunneling process involving concerted breaking of two hydrogen bonds. Second, from the observation that the splitting $\Delta\nu(A_b - A_a) \sim 1.8$ MHz (the strongest component A$_a$ occurs to the red of A$_b$), we obtain

$$-\beta_2' + \beta_2'' \sim 0.9 \text{ MHz} \quad (14)$$

neglecting β_3' and β_3''. If vibrational excitation promotes the

TABLE 8: Principal Dipole Moment Components (Permanent + Induced, in Debye) of the Dimer, Trimer, and Pentamer Calculated with the Polarization Model[a]

	dimer	trimer	pentamer
μ_a	2.61 (0.57)	0.03 (0.02)	0.31 (−0.07)
μ_b	0.08 (−0.01)	−0.20 (0.04)	0.06 (0.02)
μ_c	0.00 (0.00)	0.64 (−0.03)	0.55 (−0.02)
μ_{total}	2.61	0.67	0.64
μ_a (exptl)	2.6 [2,64]		

[a] Dipole components of tetramer and hexamer vanish due to their respective S_4 and S_6 symmetries. The induced-dipole contributions are given in the parentheses.

C_2 tunneling, i.e., $|\beta_2'| > |\beta_2''| > 0$, which is likely to be the case, then we obtain $\beta_2', \beta_2'' < 0$, assuming that the symmetry ordering remains the same in both upper and lower states. On the other hand, more restricted tunneling motion in the upper state $(0 < |\beta_2'| < |\beta_2''|)$ would yield $\beta_2', \beta_2'' > 0$. A similar set of relations also hold for β_1' and β_1'', as β_1 is close to β_2. Note that the relative ordering of the tunneling levels in Figure 7 is chosen with all the matrix elements being negative, namely, the first scenario wherein tunneling splittings increase in the excited state.

Finally, it is noteworthy that the cage hexamer exhibits a static chirality, unlike the *transient* chirality effected by the facile flipping motions in the water trimer.[34] The barrier to interconversion between the cage enatiomers is likely to be high since it requires cleavage of multiple hydrogen bonds. As such, the structural degeneracy caused by enantiotropy does not affect the present tunneling model.

In summary, the above tunneling analysis only requires that β_1 be similar to β_2 in order to fully interpret the fine triplet spectral feature observed in the VRT spectra of the cage hexamer. While this is a nonunique criterion for the structural determination, since the boat structure[25] also satisfies $\beta_1 = \beta_2$ due to the existence of two equivalent DA monomers, other important experimental evidence, especially the rotational constants reported above and the dipole moment projection measured through Stark effect presented below, supports our assignment of the observed triplet pattern to the cage form of the hexamer. We point out that the same procedure also applies to the isotopically mixed trimers containing only two homogeneous monomers, (H$_2$O)(H$_2$O)(HOD) or (D$_2$O)(D$_2$O)(HOD) or (D$_2$O)(H$_2$O)(HOD), wherein the fully resolved quartet as well as the triplet resulting from the collapsed quartet have both been observed.[37]

5. Dipole Moment Analysis. An important complementary structure characterization is provided through the molecular electric dipole moment—a measure of the electric charge distribution. The electric dipole of the water dimer has been determined to be 2.6 D along the a-axis,[64−67] which is the approximate prolate axis of the linear H-bonded cluster. It is found that the dipole moment exhibits strong K dependence (nonmonotonic behavior) but small variation with the J quantum number. A simple vector sum of the two monomer permanent moments cannot fully account for the measured μ_a. The enhancement was described by the dipole- and quadrupole-induced dipole moments and charge transfer from the proton acceptor to the proton donor.[64,68] It is to our interest to systematically investigate such enhancements of individual monomer dipoles with variations in cluster size, on the basis of an electrostatic model similar to that applied to the water dimer, and on structural and electric properties derived from experiment.

5.a. Experimental Measurements. Stark effects measured by terahertz laser spectroscopy for four pairs of asymmetry

Cage Form of the Water Hexamer

J. Phys. Chem. A, Vol. 101, No. 48, 1997 **9003**

TABLE 9: Principal Dipole Projections (in Debye) Calculated with the Polarization Model for the Nondegenerate Cage Structures[a]

		triply bonded	doubly bonded	cluster	μ_{total}
{dd}	μ_a	**1.90 (0.42)**	**0.08 (0.07)**	**1.97 (0.50)**	2.05
	μ_b	−0.84 (−0.303)	0.37 (0.38)	−0.47 (0.08)	
	μ_c	0.89 (0.55)	−0.57 (−0.59)	0.33 (−0.04)	
{du}	μ_a	**1.88 (0.40)**	**0.12 (0.08)**	**1.99 (0.49)**	2.91
	μ_b	−0.76 (−0.21)	−0.34 (0.39)	−1.10 (0.17)	
	μ_c	1.21 (0.83)	−3.02 (−0.60)	−1.81 (0.23)	
{ud}	μ_a	**1.95 (0.46)**	**0.17 (0.07)**	**2.12 (0.53)**	2.48
	μ_b	−1.03 (−0.49)	2.16 (0.40)	1.13 (−0.09)	
	μ_c	1.03 (0.70)	−1.63 (−0.59)	−0.60 (0.11)	
{uu}	μ_a	**1.94 (0.45)**	**0.08 (0.08)**	**2.02 (0.53)**	3.45
	μ_b	−0.98 (−0.45)	1.75 (0.44)	0.76 (−0.02)	
	μ_c	1.27 (0.94)	−3.97 (−0.58)	−2.70 (0.36)	
{du}*	μ_a	**1.82 (0.29)**	**−0.35 (0.07)**	**1.47 (0.36)**	1.88
	μ_b	0.91 (0.31)	0.10 (−0.45)	1.01 (−0.14)	
	μ_c	2.91 (1.02)	−3.51 (−0.88)	−0.60 (0.14)	

[a] Two groups of constituent monomers, the two flipping DA monomers (doubly bonded) and the DAA + DDA tetrameric ring (triply bonded) are reported separately. The rotational constants of these structures are given in Table 2. The induced-dipole contributions are given in the parentheses for reference.

doublets of the near prolate cage hexamer are analyzed to determine the dipole moment projections along the approximate prolate axis. The Stark energies were calculated following a treatment analogous to that of the Fermi-resonance interaction between two adjacent states, in this case the asymmetry doubling of a near symmetric rotor.[69,70] Assuming the second-order Stark contributions from levels other than the asymmetry doublet (this induces a pseudo-first-order effect) are small, this is valid as per the explanation given below, the Stark energies are

$$W^{\pm} = \frac{W_1^0 + W_2^0}{2} \pm \left[\left(\frac{W_1^0 - W_2^0}{2}\right)^2 + E^2\xi^2\right]^{1/2} \quad (15)$$

where W_1^0 and W_2^0 are the unperturbed energies of the interacting pair which can be calculated from the fitted molecular parameters listed in Table 1. The perturbation term $E^2\xi^2$ is related to the rotational line strength $\lambda a(J\tau,J\tau')$ as follows:

$$E\xi = (0.50344)E\mu_a M \left[\frac{\lambda_a(J\tau,J\tau')}{J(J+1)(2J+1)}\right]^{1/2} \quad (16)$$

The conversion factor 0.503 44 is used when the electric field is in V/cm, the dipole moment in Debye, and the resulting energy in MHz.[70] The line strengths, $\lambda a(J\tau,J\tau')$ are obtained by interpolating the tabulated values;[71] the λ's used in this work are listed in Table 5 and are based on the ground and excited states asymmetry parameters. The use of eq 15 to accurately describe the Stark pattern is ensured in the predicted first-order behavior of the Stark splittings even at low (20−40 V/cm) electric fields wherein $[(W_1^0 - W_2^0)/2] \ll E^2\xi^2$, in agreement with the observed behaviors for all the near-degenerate asymmetry doublets.

The Stark patterns observed in this work are complicated by the presence of tunneling splittings and in certain cases by the incompletely resolved individual Stark components. Special procedures are accordingly required to deconvolute the spectra. Lindfors and Cornwell[72] have demonstrated a rate-of-growth technique for the measurement of molecular dipole moments in the case of cluttered spectra, wherein the direct analysis of resolved Stark splittings is not feasible. An analogous procedure is devised here for reconstructing the splitting pattern based on the experimental line shape. First, triplicate sets of stick spectra associated with each tunneling component are calculated using

the trial dipole moments for the ground and excited states at a given value of the electric field. The spacing between successive tunneling sets is chosen to be 1.8 MHz from simulation of a field-free hexamer triplet using the same procedure described herein; the relative intensities between the three sets of line frequencies were scaled according to the nuclear spin weight ratios of 18:(6 + 6):2 and within the set scaled according to the values reported for the different M components in literature.[69] Second, a Gaussian line shape of 2.1 MHz fwhm is assumed for each line frequency. The overall superimposed Stark profile was then twice differentiated to approximate the experimental second derivative line shape resulting from the 2f lock-in detection. The 2.1 MHz Doppler line width was established through a singlet $(H_2O)_3$ absorption measurement under the identical modulation conditions employed for resolving the hexamer triplet features. The calculated peak positions are compared to the observed ones for preliminary assignments. Finally, we point out that it is the splittings between various peaks measured as a function of the electric field strength, rather than the spectral line shapes or the absolute frequencies (which are less accurate), that were fit in the nonlinear least-squares routine to yield μ_a' and μ_a''. The observed Stark splittings depend linearly on the applied electric field. To minimize the uncertainty in locating the peak positions, the "observed" splittings at any given field in the fitting routine were calculated from the first-order relations established through fitting the finite number of measurements. The uncertainties in these splittings were set between 100 and 200 kHz, spanning about 4−6 data points in a calculated spectrum; note that a simulated or an experimental singlet peak contains at least 60 data points between the two minima of the second derivative line profile.

The results are listed in Table 6. The correlation between μ_a' and μ_a'' was removed either (1) by fitting simultaneously the $\Delta M = 0$ and ± 1 Stark patterns for the same asymmetry doublet, e.g., for the P(4) transitions of $\Delta K_a = 3 \leftarrow 4$ shown in Figure 8 with individual M components clearly resolved in both cases, or (2) by fixing the μ_a values of common states between different asymmetry transitions when case 1 is infeasible, e.g., for the R(4) ($\Delta K_a = 5 \leftarrow 4$) transitions, μ_a'' was fixed to the value determined from P(4) because of their common ground states. For the R(5) transition (Figure 9) which shares no common states to other transitions studied in the Stark measurement, adding a field calibration parameter in the fit, as discussed below, fortuitously helped remove the correlation; the dipoles listed for R(5) in Table 6 were obtained by extrapolation to the point where the calibration parameter became zero. Other special constraints were also added to the nonlinear least-squares fitting routine to avoid meaningless digression of the simulated pattern from experiment regardless of a good convergence.

From the observed selection rules for the Stark patterns, one can establish the relative sign of μ_a between the ground and excited states.[73] When the perturbed wave functions corresponding to the energies $W^{\pm}$ in eq 15 are fully mixed, as is the case here, the sign of linear combination of the unperturbed wave functions depends on the sign of $\mu_a M$. As a result, the sign of dipole moment changes if the Stark transitions involving $M \neq 0$ occur between $W^+ \leftrightarrow W^-$ or $W^- \leftrightarrow W^+$ levels of the ground and excited states, but remains the same if $W \leftrightarrow W^{\pm}$ transitions take place. It is the latter case that we have observed in the present Stark measurements.

It is found that a conservative 5% (δ) error in E translates nonlinearly into a 4.6% error in μ_a' or μ_a'' for P(4). Much smaller percentage errors were observed for the dipoles determined from the other three transitions with $\delta = 5\%$: <1.7% for the R(4), <1% for the Q(5), and <0.2% for the R(5).
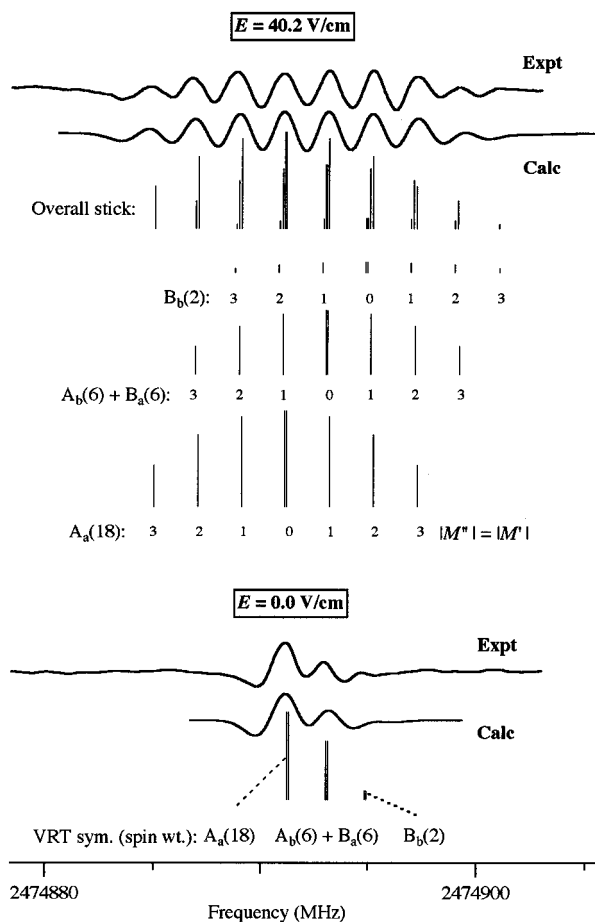
Figure 8. The fully resolved experimental and simulated $\Delta M = 0$ electric field splitting patterns of the P(4) (corresponding to $J' = K_a' = 3 \leftarrow J'' = K_a'' = 4$) VRT transitions of the cage hexamer at an electrical field of 40.2 V/cm, and the field-free patterns illustrated for comparison. Stark transitions correlating to the four tunneling symmetries (A_a, A_b, B_a, and B_b) are deconvoluted into three sets of stick spectra at each field; the middle stick spectrum contains two overlapping tunneling components ($A_b + B_a$). The observed pattern is consistent with a first-order Stark effect wherein transitions occur between the M components belonging to the same halves of the perturbed energy levels relative to the centers of the unperturbed asymmetry doublings; namely, the selection rule is upper (excited state) $\leftrightarrow$ upper (ground state) and lower $\leftrightarrow$ lower as a resulting of strong mixing between the $J = K_a + K_c$ and $K_a + K_c + 1$ levels. This suggests the same sign of μ_a in both the ground and excited states.

Therefore, we conclude that the uncertainty in the dipoles listed in Table 6 due to the lack of rigorous electric field calibration is in general less than 5%.

For the asymmetry doubling levels studied here, the contribution of the second-order Stark energy from the neighboring $|J, K_a, K_c\rangle$ states (at least 1 GHz separated from the doublets of interest) through nonzero μ_b or μ_c components amounts to less than 30 kHz splitting at the highest experimentally attainable field of 40 V/cm, 30 kHz being the interval between adjacent data points in the experimental or simulated spectra. The associated errors are thus negligible.

The cage hexamer μ_a' and μ_a'' values both exhibit strong dependence on the quantum numbers J and K_a. An attempt to obtain a unique set of the ground and excited state dipole moment components by simultaneously fitting all the Stark transitions is likely to lead to unrealistic results. In fact, such a fit was never converged.

No change in tunneling splitting upon applying an electric field was detectable in present work. This is not surprising since Stark mixing is forbidden to occur between states of different
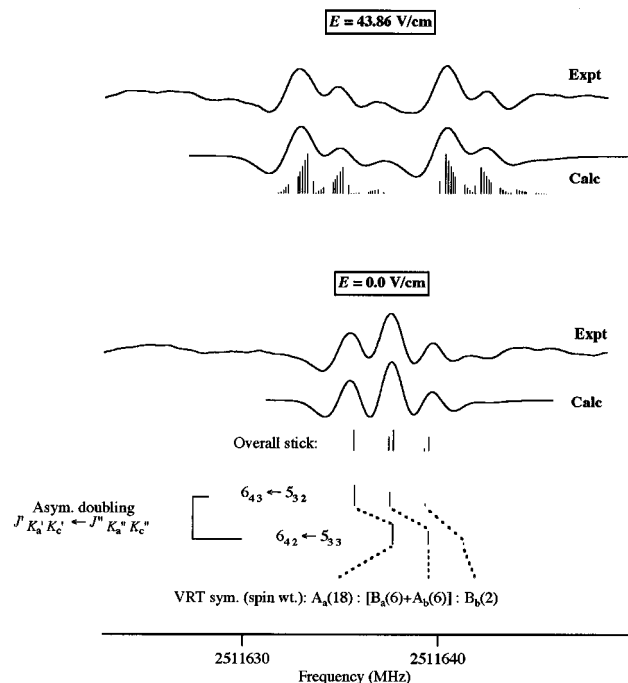
Figure 9. The partially resolved $\Delta M = \pm 1$ Stark patterns of R(5), $J' = K_a' + 2 = 6 \leftarrow J'' = K_a'' + 2 = 5$, at a field of 43.86 V/cm (upper two spectra). The asymmetry doubling was partially resolved even at the zero-field (lower two traces), leading to a prominent triplet of intensity ratios not the same as the regular 18:(6 + 6):2 tunneling pattern, but proportional to the sum of two triplets as 18:[(6 + 6) + 18]:[2 + (6 + 6)] which correlate to the symmetries A_a^{red}:[$(A_b^{red} + B_a^{red}) + A_a^{blue}$]:[$B_b^{red} + (A_b^{blue} + B_a^{blue})$] neglecting the weakest B_b^{blue} component of spin weight 2, where the superscripts denote the "red" and "blue" halves of the asymmetry doublet.

VRT symmetries A_a, A_b, B_a, and B_b according to the electric dipole selection rules derived from the MS group G_4. The absence of the Stark shifts in the tunneling splittings is a supporting piece of evidence for the absence of a symmetry-required (rather than accidental) degenerate tunneling state, such as the E state in the water dimer.[64] A symmetry required degenerate tunneling state would exhibit a first-order Stark effect, which scales as $\mu E M K / J(J + 1)$ in the symmetric top limit. For the R(5) transition reported here, this would introduce a ~1.5 MHz splitting in a degenerate state for a dipole of 1 D at a field of 40 V/cm. While a preliminary estimate, such a qualitative change should be resolvable if present in these measurements. Bemish, Chan, and Miller[74] have used dc electric fields to quench the tunneling motion in the HF dimer, but that required a large electric field (>kV/cm) such that molecular wave functions are significantly altered as a result of field-induced asymmetry imposed on the double-well potential along the tunneling coordinate. This is certainly not the case here.

5.b. Dipole Modeling. We treat the electrostatic interactions among the six polar water molecules of the cage hexamer in an induction expansion model, which includes the permanent and induced dipole moments and excludes charge-transfer effects. Each monomer has a permanent dipole vector $\boldsymbol{\mu}_i$ and a quadrupole $\mathbf{Q}_i$, both being located at the monomer center of mass $\mathbf{r}_i$. The overall dipole moment (permanent + induced) of the monomer i is[75]

$$M_i = \mu_i + \alpha_i \mathbf{E}_i \qquad (17)$$

where α_i is the polarizability tensor (also defined with respect to the monomer center of mass) and $\mathbf{E}_i$ is the field acting on the monomer i. The field $\mathbf{E}_i$ is summed over the fields from

Cage Form of the Water Hexamer

J. Phys. Chem. A, Vol. 101, No. 48, 1997 **9005**

all other monomers at the monomer i

$$\mathbf{E}_i = \sum_{j \neq i} \mathbf{E}_{ij} \qquad (18)$$

wherein $\mathbf{E}_{ij}$ is expanded through the dipole and quadrupole terms. Modifying the expression given by Gray and Gubbins,[76] we obtain

$$\mathbf{E}_{ij} = \mathbf{M}_j \mathbf{T}^{(2)}(\mathbf{r}_{ij}) - {}^1\!/_3 \mathbf{Q}_j : \mathbf{T}^{(3)}(\mathbf{r}_{ij}) \qquad (j \neq i) \quad (19)$$

where $\mathbf{r}_{ij} = \mathbf{r}_i - \mathbf{r}_j$, and $\mathbf{T}^{(2)}(\mathbf{r}_{ij}) = \nabla\nabla(1/r_{ij})$, $\mathbf{T}^{(3)}(\mathbf{r}_{ij}) = \nabla\nabla\nabla(1/r_{ij})$ with r_{ij} being the magnitude of $\mathbf{r}_{ij}$. Substituting eq 17 into 21 into eq 20 produces a set of linear equations, which must be solved in a self-consistent manner, due to the induced fields $\alpha_j \mathbf{E}_j \mathbf{T}^{(2)}(\mathbf{r}_{ij})$, to yield the converged fields $\mathbf{E}_i$. An iterative numerical procedure was found to be efficient for the present calculation. When $\mathbf{M}_j$ in eq 19 is approximated by the permanent dipole μ_j, we obtain the noniterated overall dipoles which serve as a comparison to the iterated results.

Table 7 lists the monomer structure and electric properties employed in the model. To place a monomer permanent dipole vector at the monomer center of mass, we employ a point-charge method, which is only for computational convenience since in the cluster the monomer permanent dipole vector no longer bisects the H–O–H angle because of the monomer geometry distorted from the isolated one according to ab initio calculations.[7,13,50,61,77–79] Thus, the monomer permanent dipole is calculated by assigning a point charge, $+q$, to the hydrogen atoms, $-2q$ to the oxygens. The charge $q = 1.853$ D Å^{-1} is chosen so that it reproduces the dipole (1.855 D [80]) of an isolated water molecule with the OH bond length of 0.9572 Å [81] and the bond angle of 104.52°.[81] The distorted monomer geometry listed in Table 7 produces a dipole that is artificially greater than 1.855 D of the isolated molecule. This enhancement fortuitously represents the effect of charge transfer on the dipole moment, which is not explicitly considered in the model but was found not negligible (although small) in the water dimer.[64,68] For the principal polarizability tensor components[82] and the electric quadrupole moments,[83] we used the values reported in the original papers since there are two inconsistencies found in the water dimer paper by Dyke, Mack, and Muenter.[64] The first involves the inconsistent sets of the principal axes defined between the polarizability and quadrupole tensors and the second in that the signs of the quadrupole moments were all reversed, which should not change upon the choice of axis system because the dependence of the quadrupole components on the molecular coordinates is quadratic. In this work the principal b-axis of a monomer is the C_2 axis and the c-axis is perpendicular to the molecular plane.

To examine validity of the above model, we have calculated the dipole components for the dimer, trimer, tetramer, and pentamer (Table 8) with their structures optimized to reproduce the experimental rotational constants.[3,37] The dipole projection μ_a of the water dimer has been experimentally measured[64–66,84] collectively by several groups to be 2.6 D with a perpendicular component $\mu_\perp = (\mu_b^2 + \mu_c^2)^{1/2}$ less than 0.6 D. Using our dimer model geometry, we obtain $\mu_\perp = 0.08$ and $\mu_a = 2.61$ D. The induced dipole of 0.566 D along the dimer a-axis is in close agreement with the experimental value of 0.45 ± 0.20 D determined by Dyke and co-workers.[64,84] The dipoles of the cyclic trimer, tetramer and pentamer have not been measured but were estimated to have an upper bound of 0.05 D in the molecular beam electric deflection studies,[27,28] whereas ab initio calculations at the HF level predict that the *equilibrium* dipole of the trimer, dominated by the μ_c component, is in general

less than 1.2 D.[78,79] The equilibrium S_4 structure of the tetramer will rigorously have zero dipole moment. The undetectable dipoles for the odd numbered cyclic water clusters are clearly a result of large amplitude zero-point flipping motions of the free protons, which average the asymmetric equilibrium trimer and pentamer (also including the oxygen puckering motions) to rigorously symmetric rotors.[35,41]

We now proceed to consider the dipole projection along the cluster principal a-axis, which can be directly compared with the measured μ_a values. Individual monomer contributions to this dipole component are also examined in attempt to rationalize the origin of the vibrational oscillator strength relating to the observed hybrid band types. Special attention is paid to the two groups of monomers within a cage structure: (1) the triply bonded monomers, which do not participate in the flipping motions concerned here and therefore remain common in all four cages, and (2) the two flipping DA monomers. Table 9 summarizes the μ_a dipole projections from these two groups of the molecules, as well as their combined contributions to the overall cluster dipole moment. The slightly different results among the nonflipping tetrameric rings are due to the minor adjustments of the principal axes between the cages.

As seen in Table 9, μ_a from the triply bonded monomers in all five structures are close to the values obtained in the Stark measurements. The contribution to μ_a from the DA monomers in the four structures (referred to as experimental structures below for convenience) studied in this work are less than 5%; in {du}*, the corresponding value in {du}* is slightly larger and negative in sign. Since the experimental structures reproduce the measured rotational constants better than {du}*, we believe the μ_as calculated for the former slightly better reflect the actual structure. The reason that {du}* gives poor μ_a is likely related to the lack of vibrational averaging caused by nondegenerate flipping motions in the calculation. With proper averaging considered in their DQMC calculations, Gregory and Clary[85] recently obtained $\mu = 3.0$ D and $\mu_a = 1.8$ D, in good agreement with the experimental values for μ_a, as well as with the simple model discussed in this work.

6. Trends in Water Cluster Properties: Quantifying Cooperativity. *6.a. Nearest-Neighbor Interoxygen Distance R_{O-O}.* It was previously noted in ab initio studies[6,7,77,86] that the equilibrium interoxygen distances R_{O-O} contract nearly exponentially with increasing cluster size up to the cyclic S_6 hexamer. The R_{O-O} distances calculated at the MP2 level approach the values found for liquid water and ice even at a cluster size ≥ 3. A similar behavior (Figure 10) has also been established by recent experiments for clusters up to the pentamer [3] using vibrationally averaged R_{O-O}'s obtained from model structures which reproduce the measured rotational constants. A fit of the experimental R_{O-O} distances of the dimer and cyclic clusters yields

$$R_{O-O}^{(n)} = 2.748 + 1.3 \exp(-0.8644n) \qquad (20)$$

where n is the cluster size. Such behavior is a consequence of the increasing relative contributions of many-body interactions (which are *attractive* in the cyclic hydrogen-bonded systems) to the total binding energy with increasing cluster size.[8,77,79,87–89]

For the noncyclic cage hexamer, however, the R_{O-O} distance is not expected to follow the same trend formed by the linear dimer and the quasi-planar cyclic clusters. As shown in Figure 10, the average R_{O-O} of the cage hexamer clearly deviates from the curve established for the family of cyclic clusters by +0.064 Å, compared to the value 2.756 Å extrapolated for the cyclic form. This is the manifestation of the structural transition to a 3-D hydrogen-bonded network. The definitive increase in the
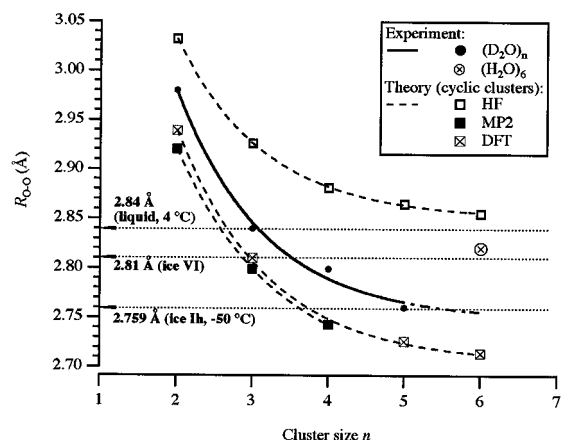
Figure 10. The experimental (vibrationally averaged) and theoretical (equilibrium),[6,7] exponentially contracting interoxygen distance R_{O-O} with the increasing water cluster size n. The experimental values[3] are obtained through model structures which reproduce the measured rotational constants. Note that, using a MC procedure[37] to simulate the vibrational averaging effect caused by the flipping motion, the trimer R_{O-O} is reduced to 2.84 Å, 0.05 Å shorter compared to the values previously reported. Although the experimental rotational constants are available only for the perdeuterated tetramer and pentamer, it is found in the case of trimer that R_{O-O}'s of different isotopic species only vary within 0.01 Å. The experimental curve is extrapolated to the cyclic hexamer to indicate the prominent deviation of R_{O-O} for its cage form. Also note that while R_{O-O}'s of the quasiplanar cyclic water clusters is converging toward that of the normal ice (Ih),[92,93] the value of 3-D cage structure resembles mostly those of the high-density polymorph of ice (VI)[101] and liquid water.[91]

interoxygen distance of the cage hexamer relative to the quasiplanar cyclic form also provides a concrete demonstration that the nonpairwise many-body contributions to the intermolecular potential are strongly dependent on geometry.[90] Indeed, ab initio calculations by Mhin et al.[19] showed that the three-body contribution to the total binding energy for the ring is 31.3% at the MP2/DZP level with basis set superposition corrections, almost 7% more than that for the cage.

Interestingly, the average (note that O—O distances vary between monomers of different bonding geometries in the cage) 2.82 Å R_{O-O} of the cage hexamer is close to the liquid water value of 2.84 Å (4 °C),[91] whereas the 2.756 Å of the cyclic S_6 hexamer resembles the 2.759 Å O—O separation measured for the ice Ih at 223 K.[92,93] The resemblance of cluster structures to those found in liquid and ice have been recognized in a number of theoretical treatments. The six-membered S_6 ring hexamer has been used to describe the hexagonal crystal bonding of ice Ih,[94,95] but extra energy is needed to pucker the isolated cyclic structure to conform to that in ice I; stabilization of this additional puckering can be provided through hydrogen bonding to the molecules surrounding the ring.[96] Moreover, such small water polygons have been implicated in computer simulation as partially accounting for the anomalous macroscopic properties of liquid water.[97−100]

Even more interestingly, the cage hexamer closely mimics the basic unit of one of the high-density polymorphs of ice, ice VI.[101,102] The cage hexamer is the central part of the unit cell, as partially illustrated in Figure 11; chains of the hexamer cage unit connected through the DA monomers run parallel to the crystal *c*-axis with four neighboring chains hydrogen-bonded laterally to each other, thereby forming the entire network of ice VI. All three types of nearest-neighbor R_{O-O} distances found in ice VI are about 2.81 Å at −175 °C, while the O···O···O angles vary from 128° (found at the joint of two cages along the chain, this angle only exists in the crystal) to as small as 76°. These parameters are nearly reproduced in the isolated
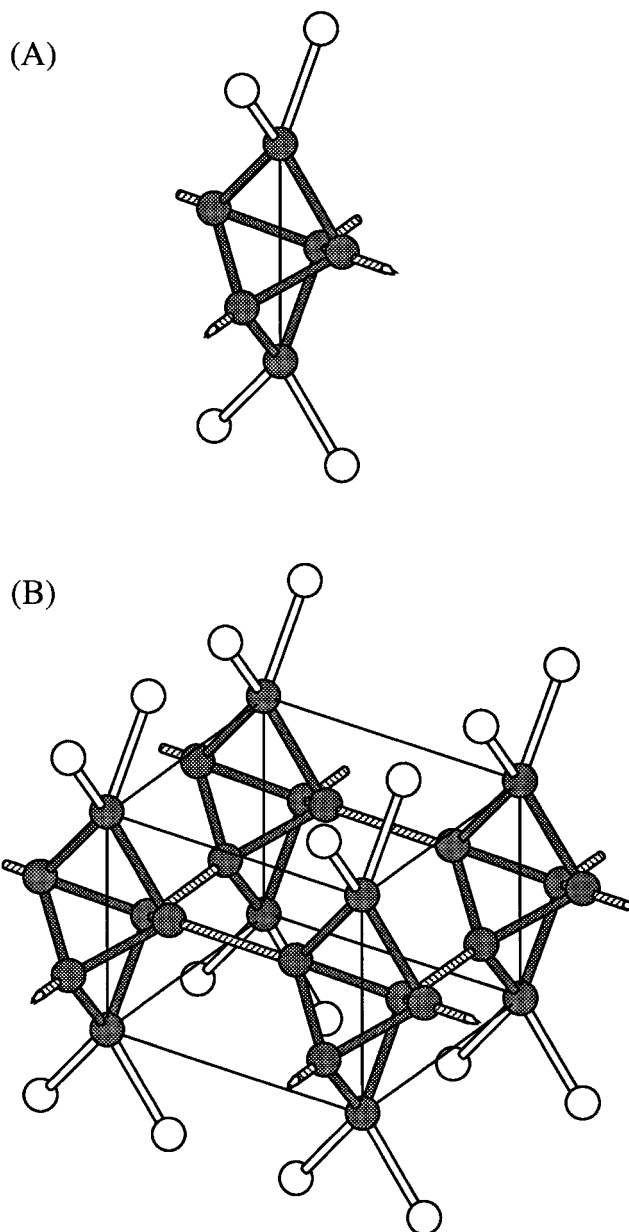
Figure 11. One of the two interpenetrating frameworks of ice VI.[101] Only the oxygen atoms (balls) are shown. Hydrogen bonds are represented by sticks. (A) The cage hexamer (shaded) is shown as the basic unit forming the hydrogen-bonded chain, which runs parallel to the crystal *c*-axis (vertical line). (B) Four such chains are linked sideways (striped sticks) to form one framework structure of ice VI. The unit cell is outlined within this framework structure. Two interpenetrating, but noninterbonded frameworks (not shown) are combined within a single cell to form the complete structure of ice VI; one framework is rotated 90° relative to the other. High density is thus achieved with the interstitial cavities of one framework accommodating those of a second.

cage hexamer with R_{O-O} being 2.82 Å and the two types of O···O···O angles being 88.71° and 77.24°.

We stress that the above numerical agreement between the cage and ice VI could be fortuitous, considering the range of R_{O-O} values in the cage—R_{O-O} varies about 3−4% according to the theoretical equilibrium structure {du}*. Nevertheless, such detailed structural similarities, especially the similar connectivity of the hydrogen bond network, constitute direct evidence for the notion that an IPS which can accurately describe the properties of small water clusters should also be able to reproduce the unusual properties of the condensed phases of water. Furthermore, the tendency for isolated water molecules

Cage Form of the Water Hexamer

J. Phys. Chem. A, Vol. 101, No. 48, 1997 **9007**

at ultralow temperatures (in a supersonic expansion) to aggregate into compact crystalline ice structures may provide a microscopic clue to the macroscopic nucleation process, wherein vapor-deposited water forms the high-density amorphous ice at low temperatures of the substrate, presumably due to insufficient thermal energy for the molecules to rearrange into the geometries corresponding to ordered crystalline forms.[103-105]

6.b. Individual Monomer Dipole Moment. Sophisticated ab initio calculations[7] can provide accurate results for the isolated water monomer dipole moment (1.855 D) which has been established through spectroscopic measurements of the Stark effect.[80] On the other hand, the dipole moment of a single water molecule in liquid at 25 °C is predicted to be 2.35, 2.18, and 2.52 D with three different empirical water–water potentials (SPC/E, TIP4P,[106] and PPC, respectively[107]). These are in agreement with the generally accepted value (2.45 D) for a water molecule in liquid at 0 °C, which decreases to 2.37 D at 83 °C, as deduced from dielectric relaxation experiments.[96,102,108] It is therefore expected that in small water clusters there exists a trend in the monomer dipole moment enhancement induced by increasing numbers of neighboring molecules. An intriguing question remains open as to the convergence of this trend to the bulk phase values; an answer to this question may elucidate the average length scale over which the cooperative H-bond interactions exist.

In parallel to the contraction in the R_{O-O} distances found in sequentially larger water clusters, a second manifestation of the hydrogen-bond cooperativity is the enhancement of the monomer dipole moment from its isolated gas-phase value of 1.855 D[80] to the 2.6 D value of ice I.[109] To quantify such effects in small water clusters, we have used the same induction expansion model to extract the dipole moments of individual monomers from the structures which establish the experimental R_{O-O} curve. The results are displayed in Figure 12 for both the iterated and noniterated results.

The enhancement in the monomer dipole found from its values in the dimer to the cyclic hexamer can also be described by an exponential function. For the iterated curve, we have

$$\mu^{(n)} = 3.13 - 1.64 \exp(-0.229n) \qquad (21)$$

where $n = 1-6$. The bond lengths and bond angles used in this calculation are given in Table 7. Two important features are readily identified. First, the monomer dipoles in the cage hexamer are smaller than the values predicted for its cyclic form and than the dipoles found in the pentamer. Second, the monomer dipole projections in the cage hexamer vary drastically from 2.23 to 2.61 D, whereas the difference between individual dipoles within the other clusters is at most 0.045 D (as in the dimer, but <0.001-0.02 D for the cyclic ones). Both are the consequence of the orientation dependence of the induced dipole, for which enhancement only occurs when the monomer dipole is favorably aligned in the electric field produced by the neighboring molecules. Recall that the average R_{O-O} of the cage is longer than the value predicted for the cyclic S_6 isomer. Together with the dipole enhancement, this seems to suggest a unifying explanation for the behavior of the cage hexamer: more restricted by the tetragonal hydrogen bonding network, the monomers in the cage are oriented less favorably for cooperative interactions (induction) than those in the quasiplanar cyclic arrangement, thereby producing a relatively longer average R_{O-O} distance and a smaller average monomer dipole than expected.

We point out that the enhancement of individual monomer dipoles does not necessarily lead to a increase in the overall *cluster* dipole, for their vector sum in the cluster-fixed axis system may be destructive, e.g., the S_4 tetramer and the S_6
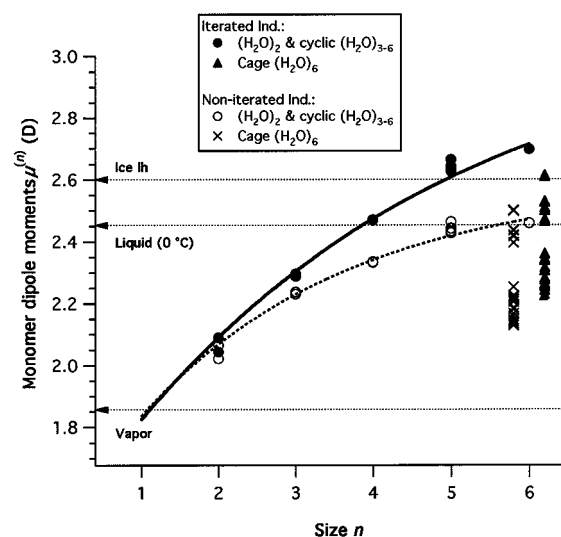
Figure 12. Exponential enhancement of individual monomer dipole moments $\mu^{(n)}$ with increasing cluster size n. The dipole moments are calculated using an induction expansion model described in the text. The monomer dipoles of the four experimental cage structures are displayed; the diffuse values of the cage (with a slight horizontal offset from the integer 6 for clarity) are due to different monomer orientations. The cage hexamer clearly shows weaker dipole moments than its cyclic form. In parallel to the trend found in R_{O-O}, the dipoles of the cyclic hexamer converge to the values of solid water[109] with a substantial (50%) enhancement from the vapor-phase dipole of 1.855 D,[80] whereas the average monomer dipole of the cage approaches that of the liquid.[96,108]

hexamer both have vanishing dipoles along the symmetric top axis even though their alternating arrangements of the monomer μ_c favor the dipole enhancement. Moreover, the structural dependence of the monomer dipole enhancements in water clusters is less sensitive than the overall cluster dipole due to the weak anisotropy in the monomer polarizability tensor (Table 7).

Finally, our calculation yielded an average dipole of 2.755 D for a fragment of ice Ih comprised of 160 molecules forming three lattice layers with each being perpendicular to the crystal *c*-axis. A second model calculation involving five water molecules arranged in a tetrahedral bonding geometry produced an enhanced dipole of 2.68 D for the central monomer. Both are substantially larger than those of the isolated clusters of sizes ≤4. The small difference between the results of the two model calculations suggests that the dipole enhancement is induced primarily by the electric field from the first tetrahedral shell, implying a spatial scale of the hydrogen-bond cooperativity on the order of a few nanometers. Note in Figure 12 that the calculated ice Ih dipole is readily reached by its gas-phase analogue, the monocyclic hexamer which has a value of 2.70 D.

IV. Discussion

Although it is predicted that the ZPE level of the cage may lie only 62 cm^{-1} below that of the prism,[25] this seemingly small separation becomes significant when compared to the low temperatures ($kT < 7$ cm^{-1}) accomplished by supersonic expansions. Direct absorption spectroscopic measurements of jet-cooled clusters therefore may offer a clue as to the relative stabilities of these nearly isoenergetic conformations. Evidence implies that Ar as a carrier gas is effective at producing the most stable structure for a given water cluster.[110] We have investigated the relative populations between two states of known energy separation using the same planar supersonic

nozzle. This was performed particularly on the R(2) and R(3) pure rotational transitions of the $(H_2O)_2$ $E^\pm$ states belonging to the upper and lower halves of the acceptor tunneling splitting ($\Delta E = 9.4$ cm^{-1} [63]). Because collisional relaxation is allowed between the $E^\pm$ symmetries, the lower $J = 2$ (E^-) and 3 (E^+), $K_a = 0$ tunneling states (signal-to-noise ratio $\sim$ 20–50) were found to be at least 1 order of magnitude more populated than the upper $E^\pm$ states of the same J, K_a quantum numbers, which is consistent with the Boltzmann factor of e$^{-\Delta E/kT}$ ($T \sim 5$ K); in fact, the upper $E^\pm$ transitions were not detected with the same sensitivity. Therefore, given the theoretical predictions and the low internal temperatures afforded by supersonic expansions, we have compiled fairly compelling evidence that the cage is the most stable form of water hexamer or it is perhaps within at most a few wavenumbers to the global ground-state structure.

A similar hexamer cage form has also been observed in the resonant ion-dip spectroscopic study of the jet-cooled benzene–$(H_2O)_6$ by Pribble and Zwier.[31] The structure assignment was established by the capability for mass selection and by the close agreement between the measured intramolecular vibrational frequencies with those calculated at the MP2 level of theory by Jordan and co-workers.[16] The fact that the same intrinsic water cluster structure has also been observed when it is weakly bound to a hydrophobic molecule also suggests that the most dominant species of water hexamer produced in supersonic expansions is indeed the cage, which should also likely be the most stable form. Other conformations and the interconversion dynamics between them remain interesting subjects to future studies.

Measurement of the donor tunneling splittings establishes the time scale of the hydrogen bond breaking and making process, which is important to truly describe the hydrogen bond network rearrangement (HBNR) dynamics within small water clusters. Ohmine and co-workers[111] have investigated the HBNR dynamics in liquid water by performing molecular dynamics (MD) simulation of a small subset of the bulk liquid. A different approach to study the dynamics in liquid water is to consider isolated clusters as a function of size and temperature, as adopted by Mukamel and co-workers.[112] It was found that a global hydrogen-bonded network structure in the liquid persists about 30 ps, a time approximately 1 order of magnitude longer than the average lifetime (2–3 ps) of the individual hydrogen bonds.[111] In the MD simulation of intermolecular vibrational spectra of water clusters by Bosma, Fried, and Mukamel,[112] longer propagation times (up to 2.1 ns) were used to generate the results. The donor tunneling splitting in the cage hexamer could be larger than the triplet line spacing (1.9 MHz) observed in our VRT spectra, since it is likely that we have measured the difference of this splitting between the ground and excited states. This suggests an even longer time scale (at least 80 ns) for computer simulations of low-temperature, large water clusters!

The induction expansion model used here to calculate the dipole moments of water clusters is a classical approach, which is known to be valid only for the electrostatic forces at long-range intermolecular separations, wherein there is little or no overlap of electron clouds.[113] At the average O–O distances in small water clusters, which correspond to an intermediate range of separations, this simplified treatment should be viewed as a convenient means of providing semiquantitative results even though the physical origin of the intermolecular forces may be incomplete. Along these lines, contributions from the higher ($>$quadrupole) multipole moments to the induced dipole in the present model were neglected, since the total dipole moment and the μ_a component of the water dimer calculated at the level

of quadrupole-induced dipole are already in good agreement with the experimental values.[2,64–66] A rigorous description of this problem should invoke quantum calculations with proper inclusion of vibrational averaging, as carried out by Gregory and Clary.[85]

Despite the accuracy of ab initio calculations on cluster structures and energetics, prediction of the vibrational frequencies, especially for the low-frequency intermolecular vibrations, is usually poor due to two factors—severe anharmonicity and mode mixing. It is likely that the vibrational band observed in this work can also be described by a low-dimensional torsional Hamiltonian, based on the argument of the flipping motions of the two DA monomers being the origin of the perpendicular transition types. Stretching of the hydrogen bonds alone without accompanying monomer torsional motions would not produce the band types observed in this experiment, nor does it seem likely that the 83 cm^{-1} (band origin) radiation energy is sufficiently high to excite the stretching motions. Following the pseudorotation model employed to treat the low-barrier torsional motions of the water trimer with reasonable success,[38,50,55,56,58,59] the vibrational problem would be in a simplified manner equivalent to that of a 2-D hindered rotation with a 4-fold asymmetric potential,[114] which links the four non-degenerate structures through flipping of the free O–H bonds on the two DA monomers, as introduced above. An experimental test of this adiabatic approximation is to search for the corresponding vibration in $(D_2O)_6$, which ought to occur at about half the vibrational frequency of $(H_2O)_6$ because its reduced internal rotation mass is approximately twice as large as that of the normal hexamer, assuming only the free protons contribute to the motion.

Attributing the observed vibration to the motions of the light hydrogens is also consistent with the small change in the $\bar{B}$ rotational constants between the ground and excited states as shown in Table 2; motions involving the heavy oxygen atoms, e.g., the hydrogen-bond stretching, would otherwise cause more than only a few MHz differences between the upper and lower states $\bar{B}$ rotational constants. Furthermore, the motions of the free O–H bonds on the doubly bonded monomers alone cannot impose the 7 MHz change in the A constant (Table 2). Such a change must also involve the motions of the hydrogen atoms further away from the a-axis.

V. Conclusions

By means of terahertz VRT laser spectroscopy, we have characterized a cage form of the normal water hexamer $(H_2O)_6$ and presented evidence for this being the lowest energy structure. Characterization of the structure and hydrogen bond network rearrangement dynamics are facilitated by the following arguments. The most definitive structural evidence is the good agreement of the precisely determined vibrationally averaged rotational constants between experiment and a DQMC simulation based on a realistic model potential. The fact that this conformation is detected in supersonically cooled (6 K) molecular jet, using both the current method of direct absorption laser spectroscopy as well as the resonant ion-dip technique,[31] supports the prediction made by both ab initio theory and DQMC simulations that the cage is the most stable form of the water hexamer. The stability of the cage is a consequence of the competition between maximizing the number of hydrogen bonds and minimizing the strains within them. Many-body (cooperative) forces are crucial in this competition, generally favoring the more open cyclic structures.

Tunneling analysis based on the cage structure has explained the triplet spectral features associated with each rovibrational

transition. Unlike the dimer and the trimer, torsional motions of the free O−H bonds ("flipping") no longer lead to degenerate tunneling pathways. An effective C_2 proton exchange within two monomers having similar bonding geometries is postulated as the tunneling mechanism giving rise to the observed triplet spectral pattern. While a boat (cyclohexane) form of the hexamer could also be consistent with the splitting pattern, this is not supported by the rotational constants or energetics, nor by the vibrational transition type, as explained below.

The donor tunneling splitting is an essential measure of the rate of the hydrogen-bond breaking and making process within water clusters, which decreases rapidly from the subnanosecond time scale found for the H_2O dimer to the submicrosecond scale for the cage $(H_2O)_6$ in the terahertz region. The corresponding splitting in $(D_2O)_6$ is expected to be much too small to be resolved. Likewise, such splitting should be very small for larger clusters, or at most comparable to that observed for the cage.

From the small differences found between the ground and excited state rotational constants, we can conclude that the motions responsible for the observed vibration originate mainly from the hydrogens, including also those on the triply bonded monomers. It is the flipping of the free hydrogens on the two doubly bonded monomers that generates dipole moment changes perpendicular to the approximate symmetry a-axis, giving rising to the observed hybrid band of both b- and c-types; the motions of the two hydrogens are also orthogonal to each other. In contrast, only one perpendicular transition type can be expected for the boat structure of the hexamer since the dipole changes caused by flipping of its two doubly bonded monomers are approximately parallel to each other, while both are perpendicular to the a-axis. To model the flipping dynamics, we propose to solve a 2-D hindered rotation problem with 4-fold asymmetric potential that links four nondegenerate structures through flipping of the two single-donor single-acceptor monomers.

The first-order Stark effect measured for the VRT transitions of the cage has allowed us to quantify the electric dipole moment projection along the molecular a-axis, thereby firmly ruling out the possibility of a cyclic (S_6) structure, which would be nonpolar. From the fully and partially resolved Stark features, we not only obtain the absolute values of μ_a in the range of 1.82−2.07 D with strong dependence on the (J,K_a) quantum numbers, but also determine that the signs of μ_a are the same for both the ground and vibrationally excited states. These values agree reasonably well with the results from an iterated induction model utilizing the cage structures deduced from the experimental rotational constants as well as that optimized from a realistic model potential. The same model also argues for the origin of the observed vibration being the flipping motions of the doubly bonded monomers. Furthermore, our model predicts that μ_a originates mainly from the triply bonded monomers; terahertz excitation is not expected to interchange the roles of proton donor and acceptor of these relatively constrained monomers, which is consistent with the fact that the same sign of μ_a has been established for both the ground and excited states.

Trends in the interoxygen distance $R_{O−O}$ and the individual monomer dipole moment have been examined for cluster sizes up to the hexamer using the measured rotational constants and the same induction model that produces the experimental dipole projections, respectively. For the linear dimer and cyclic higher clusters, the $R_{O−O}$ decreases exponentially with increasing cluster size, whereas the monomer dipole increases exponentially from 1.855 D for the isolated water molecule to 2.70 D for the cyclic

hexamer. The former is a consequence of many-body forces, the latter represents the polarization enhancement from the surrounding molecules. In both cases, the cage deviates from the trends extrapolated for the cyclic clusters; the cage average $R_{O−O}$ is longer and its monomer dipoles are less enhanced when compared with those of the ring. Together, these trends identify the cyclic-to-noncyclic structural transition, wherein the 3-D cage becomes less favored for the many-body (mainly three-body) forces than the ring, which in turn produces a smaller induced dipole.

The above two trends exhibit a rapid convergence of the cluster properties toward the bulk values. While $R_{O−O}$ and μ extrapolated for the hexamer ring are close to the values of ice Ih, there is a resemblance between these parameters determined for the cage and those of liquid water. Strong structural resemblance has also been identified between the cage and the basic unit of a high-density polymorph of ice (ice VI), not only in terms of similar hydrogen bonding networks but also their nearly identical average $R_{O−O}$ (2.82 Å for the cage and 2.81 Å for ice VI at −175 °C [101]).

In summary, this work supports the theoretical prediction that the water hexamer represents a crossover point where noncyclic structures become more stable than the cyclic isomers.[16] The quantification of the rapid evolution of molecular properties within small isolated water clusters promises to enhance our understanding of molecular interactions in bulk ice and liquid water.

Supporting Information Available: Assigned perpendicular rovibrational transitions (in megahertz) of the near prolate cage hexamer observed within the 2460−2535 GHz range (8 pages). Ordering information is given on any current masthead page.

References and Notes

(1) Fraser, G. T. *Int. Rev. Phys. Chem.* **1991**, *10*, 189.
(2) Dyke, T. R.; Muenter, J. S. *J. Chem. Phys.* **1974**, *60*, 2929.
(3) Liu, K.; Cruzan, J. D.; Saykally, R. J. *Science* **1996**, *271*, 929.
(4) Saykally, R. J.; Blake, G. A. *Science* **1993**, *259*, 1570.
(5) Del Bene, J.; Pople, J. A. *J. Chem. Phys.* **1970**, *52*, 4858.
(6) Xantheas, S. S. *J. Chem. Phys.* **1995**, *102*, 4505.
(7) Xantheas, S. S.; T. H. Dunning, J. *J. Chem. Phys.* **1993**, *99*, 8774.
(8) Kim, K. S.; Dupuis, M.; Lie, G. C.; Clementi, E. *Chem. Phys. Lett.* **1986**, *131*, 451.
(9) Farantos, S. C.; Kapetanakis, S.; Vegiri, A. *J. Phys. Chem.* **1993**, *97*, 12158.
(10) Reimers, J. R.; Watts, R. O. *Chem. Phys.* **1984**, *85*, 830.
(11) Burke, L. A.; Jensen, J. O.; Jensen, J. L.; Krishnan, P. N. *Chem. Phys. Lett.* **1993**, *206*, 293.
(12) Dykstra, C. E. *J. Chem. Phys.* **1989**, *91*, 6472.
(13) Pillardy, J.; Olszewski, K. A.; Piela, L. *J. Mol. Struct.* **1992**, *270*, 277.
(14) Jensen, J. O.; Krishnan, P. N.; Burke, L. A. *Chem. Phys. Lett.* **1995**, *241*, 253.
(15) Jensen, J. O.; Krishnan, P. N.; Burke, L. A. *Chem. Phys. Lett.* **1995**, *246*, 13.
(16) Kim, K.; Jordan, K. D.; Zwier, T. S. *J. Am. Chem. Soc.* **1994**, *116*, 11568.
(17) Tsai, C. J.; Jordan, K. D. *Chem. Phys. Lett.* **1993**, *213*, 181.
(18) Mhin, B. J.; Kim, H. S.; Kim, H. S.; Yoon, C. W.; Kim, K. S. *Chem. Phys. Lett.* **1991**, *176*, 41.
(19) Mhin, B. J.; Kim, J.; Lee, S.; Lee, J. Y.; Kim, K. S. *J. Chem. Phys.* **1994**, *100*, 4484.
(20) Laasonen, K.; Parrinello, M.; Car, R.; Lee, C.; Vanderbilt, D. *Chem. Phys. Lett.* **1993**, *207*, 208.
(21) Lee, C.; Chen, H.; Fitzgerald, G. *J. Chem. Phys.* **1994**, *101*, 4472.

(22) Vegiri, A.; Farrantos, S. C. *J. Chem. Phys.* **1993**, *98*, 4059.

(23) Franken, K. A.; Jalaie, M.; Dykstra, C. E. *Chem. Phys. Lett.* **1992**, *198*, 59.

(24) Tsoo, C.; Brooks, C. L., III *J. Chem. Phys.* **1994**, *101*, 6405.

(25) Liu, K.; Brown, M. G.; Carter, C.; Saykally, R. J.; Gregory, J. K.; Clary, D. C. *Nature* **1996**, *381*, 501.

(26) Millot, C.; Stone, A. J. *Mol. Phys.* **1992**, *77*, 439.

(27) Dyke, T. R.; Muenter, J. S. *J. Chem. Phys.* **1972**, *57*, 5011.

(28) Kay, B. D.; Castleman, A. W., Jr. *J. Phys. Chem.* **1985**, *89*, 4867.

(29) Vernon, M. F.; Krajnovich, D. J.; Kwok, H. S.; Lisy, J. M.; Shen, Y. R.; Lee, Y. T. *J. Chem. Phys.* **1982**, *77*, 47.

(30) Coker, D. F.; Miller, R. E.; Watts, R. O. *Chem. Phys.* **1985**, *82*, 3554.

(31) Pribble, R. N.; Zwier, T. S. *Science* **1994**, *265*, 75.

(32) Pugliano, N.; Saykally, R. J. *J. Chem. Phys.* **1992**, *96*, 1832.

(33) Pugliano, N.; Cruzan, J. D.; Loeser, J. G.; Saykally, R. J. *J. Chem. Phys.* **1993**, *98*, 6600.

(34) Pugliano, N.; Saykally, R. J. *Science* **1992**, *257*, 1937.

(35) Liu, K.; Loeser, J. G.; Elrod, M. J.; Host, B. C.; Rzepiela, J. A.; Pugliano, N.; Saykally, R. J. *J. Am. Chem. Soc.* **1994**, *116*, 3507.

(36) Liu, K.; Elrod, M. J.; Loeser, J. G.; Cruzan, J. D.; Pugliano, N.; Brown, M. G.; Rzepiela, J.; Saykally, R. J. *Faraday Discuss. Chem. Soc.* **1994**, *97*, 35.

(37) Liu, K.; Brown, M. G.; Viant, M. R.; Cruzan, J. D.; Saykally, R. J. special birthday issue of *Mol. Phys.* honoring A. D. Buckingham **1996**, *89*, 1373 (λ).

(38) Suzuki, S.; Blake, G. A. *Chem. Phys. Lett.* **1994**, *229*, 499.

(39) Viant, M. R.; Cruzan, J. D.; Lucas, D. D.; Brown, M. G.; Liu, K.; Saykally, R. J. *J. Phys. Chem. A* **1997**, *101*, 9032.

(40) Cruzan, J. D.; Braly, L. B.; Liu, K.; Brown, M. G.; Loeser, J. G.; Saykally, R. J. *Science* **1996**, *271*, 59.

(41) Liu, K.; Brown, M. G.; Cruzan, J. D.; Saykally, R. J. *Science* **1996**, *271*, 62.

(42) Blake, G. A.; Laughlin, K. B.; Cohen, R. C.; Busarow, K. L.; Gwo, D.-H.; Schmuttenmaer, C. A.; Steyert, D. W.; Saykally, R. J. *Rev. Sci. Instrum.* **1991**, *62*, 1701.

(43) Liu, K.; Fellers, R. S.; Viant, M. R.; McLaughlin, R. P.; Brown, M. G.; Saykally, R. J. *Rev. Sci. Instrum.* **1996**, *67*, 410.

(44) Liu, K.; Brown, M. G.; Cruzan, J. D.; Saykally, R. J. *J. Phys. Chem. A* **1997**, *101*, 9011.

(45) Brown, M. G.; Keutsch, F.; Liu, K.; Saykally, R. J., unpublished results.

(46) Owicki, J. C.; Shipman, L. L.; Scheraga, H. A. *J. Phys. Chem.* **1975**, *79*, 1794.

(47) Gregory, J. K.; Clary, D. C., private communication.

(48) Sorenson, J. M.; Gregory, J. K.; Clary, D. C. *Chem. Phys. Lett.* **1996**, *263*, 680.

(49) Wales, D. J. *J. Am. Chem. Soc.* **1993**, *115*, 11180.

(50) Schütz, M.; Bürgi, T.; Leutwyler, S.; Bürgi, H. B. *J. Chem. Phys.* **1993**, *99*, 5228.

(51) Longuet-Higgins, H. C. *Mol. Phys.* **1963**, *6*, 445.

(52) Hougen, J. T. *J. Chem. Phys.* **1962**, *7*, 1433.

(53) Bunker, P. R. *Molecular Symmetry and Spectroscopy*; Academic Press: San Diego, 1979.

(54) Dyke, T. R. *J. Chem. Phys.* **1977**, *66*, 492.

(55) Klopper, W.; Schütz, M. *Chem. Phys. Lett.* **1995**, *237*, 536.

(56) Sabo, D.; Bacic, Z.; Bürgi, T.; Leutwyler, S. *Chem. Phys. Lett.* **1995**, *244*, 283.

(57) Walsh, T. R.; Wales, D. J. *J. Chem. Soc., Faraday Trans.* **1996**, *92*, 2502.

(58) van der Avoird, A.; Olthof, E. H. T.; Wormer, P. E. S. *J. Chem. Phys.* **1996**, *105*, 8034.

(59) Olthof, E. H. T.; van der Avoird, A.; Wormer, P. E. S.; Liu, K.; Saykally, R. J. *J. Chem. Phys.* **1996**, *105*, 8051.

(60) Smith, B. J.; Swanton, D. J.; Pople, J. A.; Schaefer, H. F., III; Radom, L. *J. Chem. Phys.* **1990**, *92*, 1240.

(61) Fowler, J. E.; Schaefer, H. F., III *J. Am. Chem. Soc.* **1995**, *117*, 446.

(62) Coudert, L. H.; Hougen, J. T. *J. Mol. Spectrosc.* **1990**, *139*, 259.

(63) Zwart, E.; ter Meulen, J. J.; Meerts, W. L.; Coudert, L. H. *J. Mol. Spectrosc.* **1991**, *147*, 27.

(64) Dyke, T. R.; Mack, K. M.; Muenter, J. S. *J. Chem. Phys.* **1977**, *66*, 498.

(65) Fraser, G. T.; Suenram, R. D.; Coudert, L. H. *J. Chem. Phys.* **1989**, *90*, 6077.

(66) Hu, T. A.; Dyke, T. R. *J. Chem. Phys.* **1989**, *91*, 7348.

(67) Coudert, L. H.; Lovas, F. J.; Suenram, R. D.; Hougen, J. T. *J. Chem. Phys.* **1987**, *87*, 6290.

(68) Yamabe, S.; Morokuma, K. *J. Am. Chem. Soc.* **1975**, *97*, 4458.

(69) Townes, C. H.; Schawlow, A. L. *Microwave Spectroscopy*; Dover Publications, Inc.: New York, 1975.

(70) Gordy, W.; Cook, R. L. *Microwave Molecular Spectra*; Interscience Publishing: New York, 1970; Chapter XIII.

(71) *Microwave Spectral Tables*; National Bureau of Standards U.S. Monograph 70; National Bureau of Standards, Department of Commerce, U.S. Government Printing Office: Washington, DC, 1964; Vol. II.

(72) Lindfors, K.; Cornwell, C. D. *J. Chem. Phys.* **1965**, *42*, 149.

(73) Cotti, G.; Linnartz, H.; Meerts, W. L.; van der Avoird, A.; Olthof, E. H. T. *J. Chem. Phys.* **1996**, *104*, 3893.

(74) Bemish, R. J.; Chan, M. C.; Miller, R. E. *Chem. Phys. Lett.* **1996**, *251*, 182.

(75) Barker, J. A. *Proc. R. Soc. London, Ser. A* **1953**, *219*, 367.

(76) Gray, C. G.; Gubbins, K. E. *Theory of Molecular Fluids*; Clarence Press: Oxford, 1984; Vol. 1 (Fundamentals).

(77) Knochenmuss, R.; Leutwyler, S. *J. Chem. Phys.* **1992**, *96*, 5233.

(78) Mó, O.; Yáñez, M.; Elguero, J. *J. Chem. Phys.* **1992**, *97*, 6628.

(79) van Duijneveldt-van de Rijdt, J. G. C. M.; van Duijneveldt, F. B. *Chem. Phys.* **1993**, *175*, 271.

(80) Dyke, T. R.; Muenter, J. S. *J. Chem. Phys.* **1973**, *59*, 3125.

(81) Benedict, W. S.; Gailar, N.; Plyler, E. K. *J. Chem. Phys.* **1956**, *24*, 1139.

(82) Murphy, W. F. *J. Chem. Phys.* **1977**, *67*, 5877.

(83) Verhoeven, J.; Dymanus, A. *J. Chem. Phys.* **1970**, *52*, 3222.

(84) Odutola, J. A.; Dyke, T. R. *J. Chem. Phys.* **1980**, *72*, 5062.

(85) Gregory, J. K.; Clary, D. C.; Liu, K.; Brown, M. G.; Saykally, R. J. *Science* **1997**, *275*, 814.

(86) Honegger, E.; Leutwyler, S. *J. Chem. Phys.* **1988**, *88*, 2582.

(87) Xantheas, S. S. *J. Chem. Phys.* **1994**, *100*, 7523.

(88) Elrod, M. J.; Saykally, R. J. *Chem. Rev. (Washington, D.C.)* **1994**, *94*, 1975.

(89) Gregory, J. K.; Clary, D. C. *J. Chem. Phys.* **1996**, *103*, 8924.

(90) Xantheas, S. S. *Philos. Mag B* **1996**, *73*, 107.

(91) Narten, A. H.; Levy, H. A. *WATER: A Comprehensive Treatise*; Franks, F., Ed.; Plenum: New York, 1972; Vol. 1, pp 311−332.

(92) Peterson, S. W.; Levy, H. A. *Acta Crystallogr.* **1957**, *10*, 70.

(93) Kuhs, W. F.; Lehmann, M. S. *J. Phys. Chem.* **1983**, *87*, 4312.

(94) Yoon, B. J.; Morokuma, K.; Davidson, E. R. *J. Chem. Phys.* **1985**, *83*, 1223.

(95) White, J. C.; Davidson, E. R. *J. Chem. Phys.* **1990**, *93*, 8029.

(96) Hasted, J. B. *Aqueous Dielectrics*; Chapman and Hall: London, 1973.

(97) Speedy, R. J. *J. Phys. Chem.* **1984**, *88*, 3364.

(98) Stillinger, F. H. *Science* **1980**, *209*, 451.

(99) Belch, A. C.; Rice, S. A. *J. Chem. Phys.* **1987**, *86*, 5676.

(100) Corongiu, G.; Clementi, E. *J. Chem. Phys.* **1993**, *98*, 2241.

(101) Kamb, B. *Science* **1965**, *150*, 205.

(102) Eisenberg, D.; Kauzmann, W. *The Structure and Properties of Water*; Oxford University: New York, 1969.

(103) Jenniskens, P.; Blake, D. F.; Wilson, M. A.; Pohorille, A. *Astrophys. J.* **1995**, *455*, 389.

(104) Mishima, O.; Calvert, L. D.; Whalley, E. *Nature* **1984**, *310*, 393.

(105) Hagen, W.; Tielens, A. G. G. M.; Greenberg, J. M. *Chem. Phys.* **1981**, *56*, 367.

(106) Jorgensen, W. L.; Chandrasekhar, J.; Madura, J. D.; Impey, R. W.; Klein, M. L. *J. Chem. Phys.* **1983**, *79*, 926.

(107) Kusalik, P. G.; Svishchev, I. M. *Science* **1994**, *265*, 1219.

(108) Haggis, G. H.; Hasted, J. B.; Buchanan, T. J. *J. Chem. Phys.* **1952**, *20*, 1452.

(109) Coulson, C. A.; Eisenburg, D. *Proc. R. Soc. London, Ser. A* **1966**, *291*, 454.

(110) Emilsson, T.; Germann, T. C.; Gutowsky, H. S. *J. Chem. Phys.* **1992**, *96*, 8830.

(111) Ohmine, I.; Tanaka, H. *Chem. Rev. (Washington, D.C.)* **1993**, *93*, 2545.

(112) Bosma, W. B.; Fried, L. E.; Mukamel, S. *J. Chem. Phys.* **1993**, *98*, 4413.

(113) Maitland, G. C.; Rigby, M.; Smith, E. B.; Wakeham, W. A. *Intermolecular Forces: Their Origin and Determination*; Clarendon Press: Oxford, 1981.

(114) Lister, D. G.; MacDonald, J. N.; Owen, N. L. *Internal Rotation and Inversion: An Introduction to Large Amplitude Motions in Molecules*; Academic Press: London, 1978.